



UNIVERSITÀ  
DEGLI STUDI  
FIRENZE

# FLORE

## Repository istituzionale dell'Università degli Studi di Firenze

### **Extended classification of surface errors shapes in peripheral end-milling operations**

Questa è la Versione finale referata (Post print/Accepted manuscript) della seguente pubblicazione:

*Original Citation:*

Extended classification of surface errors shapes in peripheral end-milling operations / Morelli L.; Grossi N.; Scippa A.; Campatelli G.. - In: JOURNAL OF MANUFACTURING PROCESSES. - ISSN 1526-6125. - ELETTRONICO. - 71:(2021), pp. 604-624. [10.1016/j.jmapro.2021.09.054]

*Availability:*

The webpage <https://hdl.handle.net/2158/1256509> of the repository was last updated on 2022-02-16T15:55:53Z

*Published version:*

DOI: 10.1016/j.jmapro.2021.09.054

*Terms of use:*

Open Access

La pubblicazione è resa disponibile sotto le norme e i termini della licenza di deposito, secondo quanto stabilito dalla Policy per l'accesso aperto dell'Università degli Studi di Firenze (<https://www.sba.unifi.it/upload/policy-oa-2016-1.pdf>)

*Publisher copyright claim:*

Conformità alle politiche dell'editore / Compliance to publisher's policies

Questa versione della pubblicazione è conforme a quanto richiesto dalle politiche dell'editore in materia di copyright.

This version of the publication conforms to the publisher's copyright policies.

La data sopra indicata si riferisce all'ultimo aggiornamento della scheda del Repository FloRe - The above-mentioned date refers to the last update of the record in the Institutional Repository FloRe

(Article begins on next page)



# Extended classification of surface errors shapes in peripheral end-milling operations

Lorenzo Morelli\*, Niccolò Grossi, Antonio Scipia, Gianni Campatelli

Department of Industrial Engineering, University of Firenze, via di Santa Marta 3, 50139 Firenze, Italy

## ARTICLE INFO

### Keywords:

Milling  
Cutting forces  
Simulation  
Surface analysis  
Form error

## ABSTRACT

The prediction of form surface error represents the basis of many approaches, which aims at increasing the productivity and reducing the costs of a milling operation. In peripheral end-milling the form error caused by the tool/workpiece static deflection is not constant along the axial depth of cut, and it presents different shapes due to the cutting forces, which change according to the cutting strategy, end-mill geometry and cutting parameters, making the surface error prediction complex and time consuming. This paper presents a comprehensive classification of the shape of the cutting forces which cause the surface form errors, in both up and down-milling. The proposed classification includes analytical equations to obtain the axial position of key points (also known as kinks) defining the surface error shape in any cutting condition and tool geometry. The results given by the developed classification were experimentally validated through different cutting tests to prove the reliability and the effectiveness of the proposed approach. The proposed classification and formulations manage to identify the surface error shapes both when several flutes are involved in the process and aggressive axial depths of cut are adopted, extending the knowledge about surface errors in peripheral milling. Furthermore, the proposed formulations could be exploited to ease error prediction methods based on simulations or drastically reduce the surface measuring time in quality control.

## 1. Introduction

In the modern vision of milling operations, one of the most challenging tasks is finding the optimal compromise between the required accuracy and the maximization of process productivity [1]. For this purpose, surface error prediction is becoming more and more important [2] since it is at the base of many approaches which aim at increasing milling productivity saving the manufacturing cost. For example, the predicted surface error helps cutting parameters preselection [3] as well as the application of compensation strategies to the original toolpath of the milling cycle [4]. As well as this, the predicted surface error supports the calculation of an optimal cutting sequence [5] to improve the effectiveness of the original toolpath. On the other hand, the predicted surface error is also suitable for monitoring systems [6] in which the magnitude of the predicted surface error is used to control the accuracy of the machined surface. Focusing on peripheral end-milling operations, several approaches predict the surface error, considering both dynamic aspects (e.g. vibrations [7–9]) and static aspects (e.g. tool deflection [10,11]). Dynamic mechanisms impact on the machined surface mostly at the roughness level [12], instead static mechanisms affect the ma-

chined surface mainly at the form level [13]. Most of the works on this topic are focused on error prediction, often using numerical methods [14], while few [15–17] are dedicated to investigating and classifying the error shapes assumed by surface at different cutting conditions. This paper provides an extensive investigation and a comprehensive classification of the forms of surface error caused by the tool deflection to support error prediction, quality control and process planning. Indeed, in peripheral milling operations the surface error assumes a certain shape along the axial depth of cut [18,19]. This shape depends on the cutting forces acting on the workpiece during the surface generation (i.e., surface generating force) [20] and it presents some key points whose axial positions are related to the cutting parameters, cutting strategy and tool geometry [21]. These points are also referred to as kinks, and they allow the identification of the zones where the surface error assumes maximum and minimum values. For this reason, their knowledge is important to describe the form of the surface errors. In literature, some studies have faced the problem of finding the key points to define the form of surface error in peripheral milling operations. Woo-Soo Yun et al. [22] presented an analytical equation for the axial position of the key point corresponding to the peak value of the surface generating

\* Corresponding author.

E-mail address: [lorenzo.morelli@unifi.it](mailto:lorenzo.morelli@unifi.it) (L. Morelli).

force. The equation proposed is reliable, but it is limited to very few cutting conditions. M. N. Islam et al. [15] proposed analytical expressions for the axial position of four key points, considering a different range of cutting conditions and the tool stiffness through an elastic beam model. Despite the extended number of key points shown, the range of cutting conditions analyzed is not enough to reconstruct a comprehensive picture of the key points characterizing the form of the surface error. Chang et al. [23] described the generating mechanism and formation criteria for kinks in peripheral milling covering both down-milling and up-milling operations. The authors distinguished various surface error shapes and proposed analytical equations for the axial positions of the kinks in different cutting conditions. The study proved that the form of surface error is not unique, and it changes from down-milling to up-milling. However, the range of conditions investigated by the authors is limited to cutting operations with only two flutes cutting simultaneously, making the results obtained not suitable for cutting operations with high axial depths of cut, and several flutes involved in the cut. Desai et al. [16], starting from the force classification developed by Liuqing Yang et al. [24], also identified various surface error shapes, each one defined by its own key points whose axial positions were provided with dedicated equations. The results of the authors extended the results proposed by Chang et al., nonetheless the number of types of surface error shapes considered is partial. Indeed, the authors focused their attention on down milling operations with only two flutes cutting simultaneously and just in certain cutting conditions. Therefore, the effectiveness of the expressions proposed for the key points is limited to specific cases. The aim of this paper is to provide a comprehensive picture of the forms of the surface error caused by the tool static deflection in peripheral end-milling, covering both down-milling and up-milling strategies. To achieve such a goal, this study first classifies the shapes of the cutting forces for every feasible cutting condition considering the influence of both the number of flutes (i.e., overlap) and the tool's helix angle, then for each shape analytical equations are provided to predict the axial position of the key points characterizing the form of the surface error. An extensive experimental validation is presented in Section 4 to show the effectiveness of the proposed equations. The proposed formulations are effective in describing the surface error shapes in different cutting conditions both when several flutes are cutting simultaneously and aggressive axial depths of cut are adopted, extending the results found in previous works. These formulations are meant to be a new tool to support error prediction, quality control and cutting parameters preselection. As an example, the proposed formulations are paired with an established tool deflection model to efficiently predict surface error.

## 2. Machined surface generation

In peripheral milling, the cutting process starts each time a flute of the endmill reaches the entry angle  $\phi_{in}$  by entering the workpiece, and it finishes as soon as the same flute passes the exit angle  $\phi_{out}$  leaving the workpiece. Nonetheless the machined surface is generated only in a specific moment of this interval, that is when the flute is orthogonal to the workpiece surface. Based on the cutting strategy, the flute reaches this surface generation position at the exit angle ( $\pi$ ) for down-milling operations (Fig. 1a) and at entry angle (0) for up-milling operations (Fig. 1b).

Moreover, the instant, that a flute reaches the position of surface generation, varies continuously along the axial depth of cut ( $ap$ ) because the helix of the endmill changes the flute location along the tool axis. As a result, introducing  $\alpha_{sw}$ , as the axial engagement angle, the surface generation starts at the bottom of  $ap$  at  $\phi_{out}$ , and it finishes at the top of  $ap$  of cut at  $\phi_{out} + \alpha_{sw}$  for down-milling operations (Fig. 1a); instead, for up-milling operations, the surface generation starts at the bottom of  $ap$  at  $\phi_{in}$  and it finishes at the top of  $ap$  at  $\phi_{in} + \alpha_{sw}$  (Fig. 1b); however, in both cases the axial engagement angle  $\alpha_{sw}$  is related to  $ap$  and to the endmill's geometry following the equations:

$$\alpha_{sw} = k_b ap \quad (1)$$

$$k_b = \frac{2 \tan(\alpha_{el})}{D} \quad (2)$$

where  $\alpha_{el}$  is the tool helix angle and  $D$  is the tool diameter. It must be noted that the axial engagement angle is obtained assuming a constant value for the tool helix angle, therefore Eqs. (1) and (2) are not suitable for endmills with highly variable helix angle.

In summary, the overall machined surface is generated gradually in a certain range of angular positions therefore using the engagement angle  $\vartheta$  as variable the surface generation range may be expressed with these relations:

$$\phi_{out} \leq \vartheta \leq \phi_{out} + \alpha_{sw} \text{ (down - milling)} \quad (3)$$

$$\phi_{in} \leq \vartheta \leq \phi_{in} + \alpha_{sw} \text{ (up - milling)} \quad (4)$$

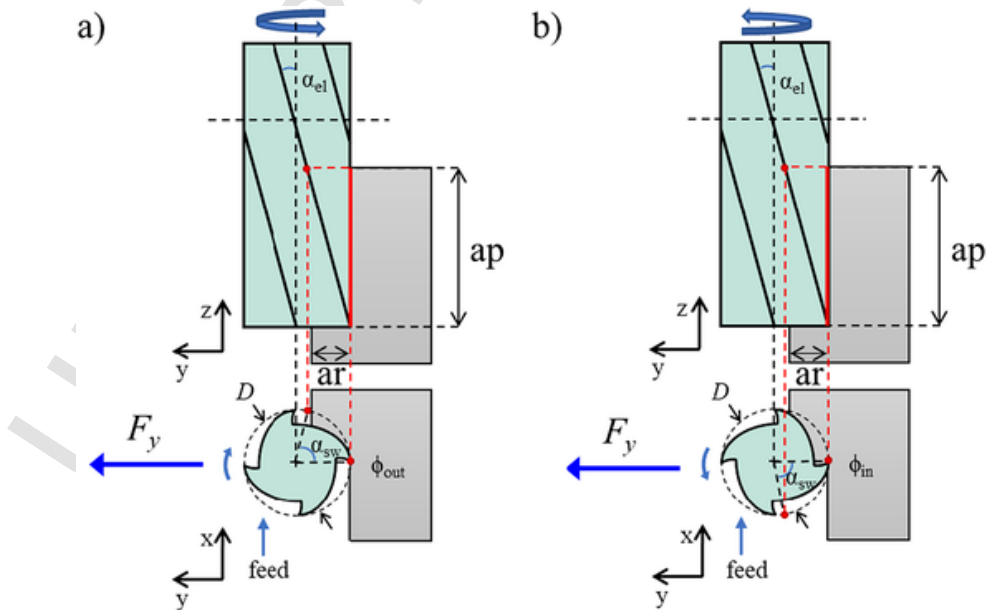


Fig. 1. Surface generation position: a) down-milling b) up-milling.

Surface errors are dominated by the tool's deflections in the direction normal to the machined surface (y-axis), thus the analysis of the resultant of the cutting forces along the y-direction  $F_y$  (normal to the surface as shown in Fig. 1) [20] becomes essential to describe the surface error shape. In detail, surface errors are related to the magnitude of  $F_y$  acting on the tool during the surface generation process, which is identified by the surface generation range. Therefore, the portion of  $F_y$  enclosed within the surface generation range is referred to as “surface generating force”, and it represents the cutting force responsible for surface errors. Due to the tool helix angle, for each position of the surface generation range, the flute creating the surface assumes a different position along the axial depth of cut, and it is subjected to a different value of the surface generating force (Fig. 2). Thus, by knowing the shape of the surface generating force, the main characteristics (i.e., key points) of the surface error shape may be obtained.

### 3. Proposed approach

The shape of the surface generating force presents some key points which also appear in the surface error shape. These points are related to the  $F_y$  shape, which is not unique, but it changes according to the cutting strategy (down-milling or up-milling), the cutting parameters (radial depth of cut  $ar$ , axial depth of cut  $ap$ ) and the tool geometry (tool diameter  $D$ , helix angle  $\alpha_{el}$ , number of flutes  $N$ ). Therefore, to fully analyze all the possible shapes which  $F_y$  may assume, the  $F_y$  shape was first classified considering a single fluted endmill ( $N = 1$ ) then the obtained classification was extended to a general multiple fluted endmill ( $N > 1$ ) as in [16,24]. For every identified shape, the angular positions of the key points characterizing the  $F_y$  shape were estimated through analytical expressions. These angular positions, referred to as key angles, defines the  $F_y$  shape in one period  $\phi_z$  wide (cutting force periodicity), where  $\phi_z$  is the tool pitch angle. Assuming a constant pitch between the flutes, the pitch angle ( $\phi_z$ ) is defined by the following equation:

$$\phi_z = 2\pi/N \quad (5)$$

#### 3.1. Single fluted endmill force shape classification

In this section a classification of the  $F_y$  shapes for a single fluted endmill ( $N = 1$ ) is presented. To achieve such goal, a set of working angles is defined to analyze the effects of both cutting parameters ( $ar$ ,  $ap$ ) and tool geometry ( $D$ ,  $\alpha_{el}$ ) on the  $F_y$  shape. Starting from  $ar$ , the radial engagement angle  $\alpha_{en}$  for both down-milling and up-milling is defined with the following equation as in [16,24]:

$$\alpha_{en} = \phi_{out} - \phi_{in} = \arccos(1 - 2ar/D) \quad (6)$$

For both  $\alpha_{en}$  and  $\alpha_{sw}$ , a critical value is defined in order to consider their effects on the  $F_y$  shape; in particular, the critical axial engagement angle  $\alpha_{swc}$  is the axial engagement angle that equals  $\alpha_{en}$  (Eq. (7)) as in [24].

$$\alpha_{swc} = \alpha_{en} \quad (7)$$

In addition, the critical radial engagement angle  $\alpha_{enc}$  is defined as the radial engagement angle which identifies the angular position of the maximum of  $F_y$  in a slotting condition. It must be noted that  $\alpha_{enc}$  is not related to the maximum chip thickness because this analysis focused on  $F_y$  which is resultant of the cutting forces along the y-direction. Indeed, the peak value of  $F_y$  depends on how the tangential cutting force  $F_t$  and the radial cutting force  $F_r$  combine along the y-direction during the cutting process. Therefore, the adoption of a cutting model is essential to predict  $\alpha_{enc}$ . In this analysis, a simple mechanistic cutting model (8, 9, 10) analogous to the one used in other works [25–27], is considered.

$$h = fz \sin(\theta) \quad (8)$$

$$F_t = K_{tc}hb \quad (9)$$

$$F_r = K_{rc}hb \quad (10)$$

where  $h$  is the chip thickness,  $fz$  is the feed per tooth,  $K_{tc}$  and  $K_{rc}$  are respectively the tangential and the radial cutting coefficients while  $b$  is the chip width.

Thanks to the cutting model considered, two analytical expressions for  $\alpha_{enc}$  were developed, one for down-milling (11) and one for up-milling (12).

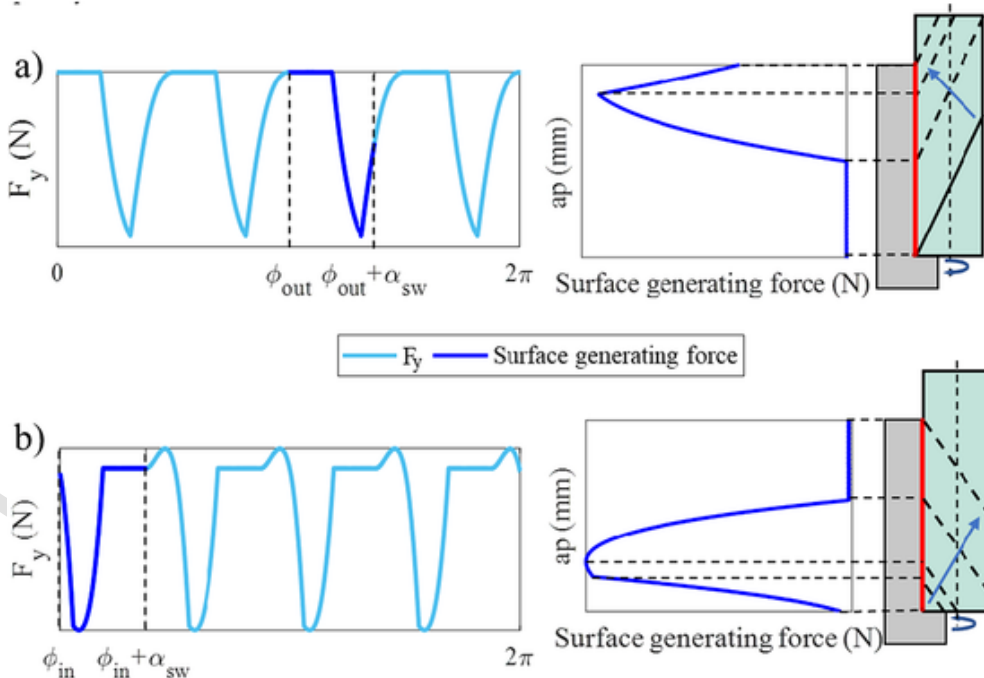


Fig. 2. Example of axial surface generating force profile a) Down-Milling b) Up-milling.

$$\alpha_{enc} = \frac{\alpha_{sw}}{2} + \operatorname{atan} \left( \frac{\sqrt{K_{tc}^2 + K_{rc}^2} + K_{tc}}{K_{rc}} \right) \quad (11)$$

$$\alpha_{enc} = \pi + \frac{\alpha_{sw}}{2} - \operatorname{atan} \left( \frac{\sqrt{K_{tc}^2 + K_{rc}^2} + K_{tc}}{K_{rc}} \right) \quad (12)$$

The accuracy of these expressions (11, 12) is related to the accuracy of the cutting model considered; nonetheless, the use of these expressions can be extended to more complex cutting models. To fully describe the effects of  $ar$  and  $ap$  on the  $F_y$  shape, an additional radial engagement angle  $\alpha_{enu}$  is defined for up-milling (13).

$$\alpha_{enu} = \alpha_{sw} + \operatorname{atan} (K_{rc}/K_{tc}) \quad (13)$$

$\alpha_{enu}$  represents the radial engagement angle which fixes the angular position of the peak value of  $F_y$ , and it depends on how  $F_t$  and  $F_r$  combine along the y-direction in the final instants of the cut. Moreover, the expression (13) present the same limitations of Eqs. (11) and (12) due to its dependency on the cutting model considered. Secondly, the working angles described (Eqs. (1), (6), (7), (11), (12), (13)) are used to define all the key angles which describe the  $F_y$  shape in one period for a single fluted endmill. The angles  $\alpha_{sw}$  and  $\alpha_{en}$  are used to define the key angles common to both down-milling and up-milling operations with the following equations:

$$\vartheta_1 = \phi_{in} \quad (14)$$

$$\vartheta_2 = \phi_{in} + \alpha_{en} \quad (15)$$

$$\vartheta_3 = \phi_{in} + \alpha_{sw} \quad (16)$$

$$\vartheta_4 = \phi_{in} + \alpha_{sw} + \alpha_{en} \quad (17)$$

Additional specific key angles for down-milling and up-milling are defined using  $\alpha_{enc}$  and  $\alpha_{enu}$ :

$$\vartheta_M = \phi_{in} + \alpha_{sw} + \alpha_{en} - \alpha_{enc} \text{ (down – milling)} \quad (18)$$

$$\vartheta_M = \phi_{in} + \alpha_{enc} \text{ (up – milling)} \quad (19)$$

$$\vartheta_m = \phi_{in} + \alpha_{enu} - \alpha_{sw} \text{ (up – milling)} \quad (20)$$

$$\vartheta_u = \phi_{in} + \alpha_{enu} \text{ (up – milling)} \quad (21)$$

The key angles  $\vartheta_1$  and  $\vartheta_2$  represent respectively the cutter entry angle  $\phi_{in}$  and cutter exit angle  $\phi_{out}$  at the bottom of  $ap$ . Analogously,  $\vartheta_3$  and  $\vartheta_4$  represent respectively the cutter entry angle  $\phi_{in}$  and cutter exit angle  $\phi_{out}$  at the top of  $ap$ . On the other hand, for both down-milling and up-milling,  $\vartheta_M$  identifies the angular position of the maximum of  $F_y$  in cutting operations with high radial depths of cut (Fig. 3). Instead,  $\vartheta_m$  and  $\vartheta_u$  are specific for up-milling operations, and  $\vartheta_m$  corresponds to the minimum of  $F_y$  while  $\vartheta_u$  is related to the maximum of  $F_y$  in cutting operations with high axial depths of cut (Fig. 4). In down-milling operations,  $\vartheta_m$  and  $\vartheta_u$  are not present because the contribute of  $F_t$  and  $F_r$  along the y-direction changes significantly with the cutting strategy. It must be also noted that the relations for  $\vartheta_1$ ,  $\vartheta_2$ ,  $\vartheta_3$  and  $\vartheta_4$  depend only on the tool's geometry ( $\alpha_{el}$ ,  $D$ ) and the cutting parameters ( $ar$ ,  $ap$ ) while the ones for  $\vartheta_m$  and  $\vartheta_M$  are also affected by the cutting coefficients ( $K_{tc}$ ,  $K_{rc}$ ). Furthermore, these equations provide enough information to describe also the  $F_y$  shape in any peripheral milling operation with a single flute involved in the cut.

Nonetheless, depending on the cutting parameters ( $ar$ ,  $ap$ ) not every key angle is necessary to describe the  $F_y$  shape. Indeed, based on the relative magnitudes of  $\alpha_{sw}$  and  $\alpha_{en}$ , which are related to  $ap$  and  $ar$  respectively, the shape of  $F_y$  may significantly change. Therefore, to distinguish all the possible  $F_y$  shapes and their corresponding key angles, a comprehensive comparison between  $\alpha_{en}$ ,  $\alpha_{sw}$  and their critical values ( $\alpha_{enc}$ ,  $\alpha_{enu}$  and  $\alpha_{swc}$ ) is conducted. Thanks to this method, three types of  $F_y$  shape are identified for both down-milling and up-milling:

- Type I: This triangle-like shape is typical of cutting operations which uses conservative cutting parameters, and it always features  $\alpha_{en}$  greater than  $\alpha_{sw}$ . In down-milling, type I is characterized by

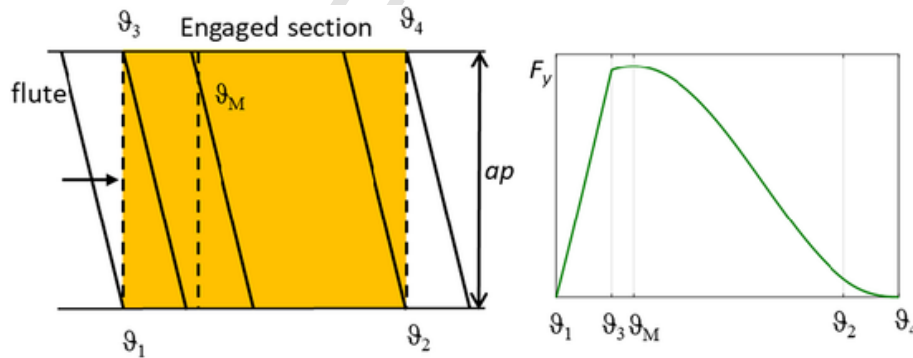


Fig. 3. Example of key angles for a down-milling operation.

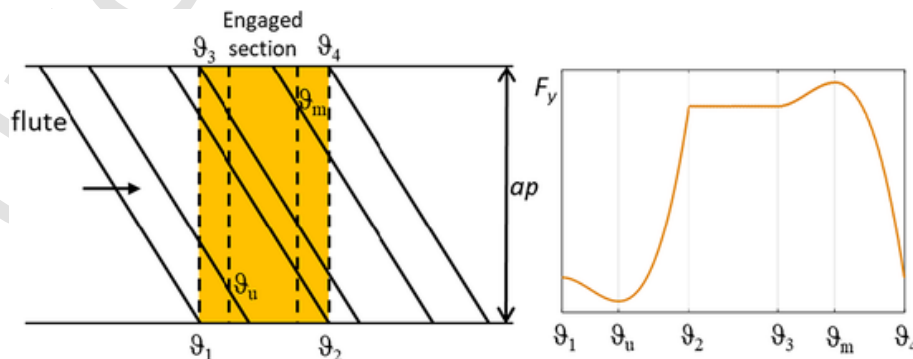


Fig. 4. Example of key angles for an up-milling operation.



three key angles:  $\theta_1$ ,  $\theta_3$ ,  $\theta_4$ , with  $\theta_3$  peak of  $F_y$ . Two subtypes (Ia, Ib) are considered based on the magnitude of  $\alpha_{en}$  which changes the proportion between the rising edge, from  $\theta_1$  to  $\theta_3$ , and the falling edge, from  $\theta_3$  to  $\theta_4$ . In up-milling, the additional angle  $\theta_m$  is introduced to include the  $F_y$  minimum typical of this operation, and in case of Ib (occurring with high values of  $\alpha_{sw}$ ) also the angle  $\theta_u$  must be considered to identify the peak of  $F_y$ .

- Type II: This trapezoidal force shape occurs in cutting operations with aggressive axial depths of cut, and it always features  $\alpha_{sw}$  greater than  $\alpha_{enc}$ . Type II is characterized by four key angles:  $\theta_1$ ,  $\theta_2$ ,  $\theta_3$ ,  $\theta_4$ , with the same two additional angles in up-milling:  $\theta_m$  and  $\theta_u$ . The difference between type IIa and type IIb is not significant for a single fluted endmill, but it changes the  $F_y$  shape for a multiple fluted endmill as it will be described in the next section.
- Type III: This profile identifies cutting operations with aggressive radial depths of cut, and it presents  $\alpha_{en}$  greater than  $\alpha_{enc}$ . Type III is defined by four key angles:  $\theta_1$ ,  $\theta_3$ ,  $\theta_M$ ,  $\theta_4$ . In up-milling,  $\theta_m$  is added as for the other types.

Force profile types are summarized in Table 1 with their occurrence conditions, and force profile examples are shown in Fig. 5, while characteristic key angles for one period (from  $\theta_1$  to  $\theta_1 + \phi_z$  in down-milling and from  $\theta_4 - \phi_z$  to  $\theta_4$  in up-milling) are provided in Table 2. It must be noted that both the critical radial engagement angles  $\alpha_{enu}$  and  $\alpha_{enc}$  are related to  $\alpha_{sw}$  (11, 12, 13), but the critical axial engagement angle  $\alpha_{swc}$  depends on  $\alpha_{en}$  (7) therefore a cutting operation characterized by  $\alpha_{en} > \alpha_{enc}$  and  $\alpha_{sw} > \alpha_{swc}$  cannot occur.

The types described for both down and up milling identify all the possible  $F_y$  shapes in one period for a single fluted endmill. They are also suitable for any peripheral milling operation in which only one

flute is involved in the cut. Nonetheless, milling operations are usually characterized by several flutes cutting simultaneously therefore this first classification must be extended to a general multiple fluted endmill ( $N > 1$ ).

### 3.2. Multiple fluted endmill force shape classification

In the previous section all the possible shapes, which  $F_y$  may assume for a single fluted endmill, were classified in types. In this section, the influence of the number of flutes  $N$  on  $F_y$  shape was investigated extending the type classification for a single fluted endmill to a multiple fluted endmill ( $N > 1$ ). Indeed, the shape of  $F_y$  for a multiple fluted endmill can be described as the combination of multiple single flute  $F_y$  shapes as it is shown in Fig. 6 for a four fluted endmill.

From this perspective the multiple flutes  $F_y$  shape can be classified by evaluating how single flute  $F_y$  shapes of the same type may interact one another. Thus, to describe these interactions the amount of overlap between two single flute  $F_y$  shapes was adopted. Considering the features of each type described in Section 3.1, six different degrees of overlap (Fig. 7) were classified:

- No Overlap: This configuration applies to all the types of single flute  $F_y$  shape, and it verifies when the previous and the following single flute  $F_y$  shapes do not interact with one another.
- Low Overlap (L): The low overlap condition applies to all the types of single flute  $F_y$  shape as well. In detail, the low overlap occurs when the falling edge of the previous single flute  $F_y$  shape influences only the rising edge of the following single flute  $F_y$  shape.
- Medium Overlap (M): This condition applies to all the types of single flute  $F_y$  shape like the others. However, in this case the falling edge of the previous single flute  $F_y$  shape affects two edges, rising and falling edge (type Ia, type Ib, type III) or rising and constant portion (type IIa, type IIb), of the following single flute  $F_y$  shape.
- High Overlap (H): The high overlap condition applies to type Ia, Ib, IIa and III. In detail the high overlap occurs when the rising edge of the previous single flute  $F_y$  shape affects the rising edge of the following single flute  $F_y$  shape.
- Deep medium overlap (m): The deep medium overlap occurs only for type IIb. In this case the falling edge of the previous single flute  $F_y$  shape influences the constant portion of the following single flute

**Table 1**  
Single flute  $F_y$  profile conditions.

	Ia	Ib	IIa	IIb	III
Down-milling	$\alpha_{en} < \alpha_{enc}$ $\alpha_{sw} \leq \alpha_{swc}$ $\alpha_{en} < 2\alpha_{swc}$	$\alpha_{en} < \alpha_{enc}$ $\alpha_{sw} \leq \alpha_{swc}$ $\alpha_{en} \geq 2\alpha_{swc}$	$\alpha_{en} < \alpha_{enc}$ $\alpha_{sw} > \alpha_{swc}$ $\alpha_{en} < 2\alpha_{swc}$	$\alpha_{en} < \alpha_{enc}$ $\alpha_{sw} > \alpha_{swc}$ $\alpha_{en} \geq 2\alpha_{swc}$	$\alpha_{en} \geq \alpha_{enc}$ $\alpha_{sw} \leq \alpha_{swc}$
Up-milling	$\alpha_{en} \leq \alpha_{enc}$ $\alpha_{sw} \leq \alpha_{swc}$ $\alpha_{en} \geq \alpha_{enu}$	$\alpha_{en} \leq \alpha_{enc}$ $\alpha_{sw} \leq \alpha_{swc}$ $\alpha_{en} < \alpha_{enu}$	$\alpha_{en} < \alpha_{enc}$ $\alpha_{sw} > \alpha_{swc}$ $\alpha_{en} < 2\alpha_{swc}$	$\alpha_{en} < \alpha_{enc}$ $\alpha_{sw} > \alpha_{swc}$ $\alpha_{en} \geq 2\alpha_{swc}$	$\alpha_{en} \geq \alpha_{enc}$ $\alpha_{sw} \leq \alpha_{swc}$

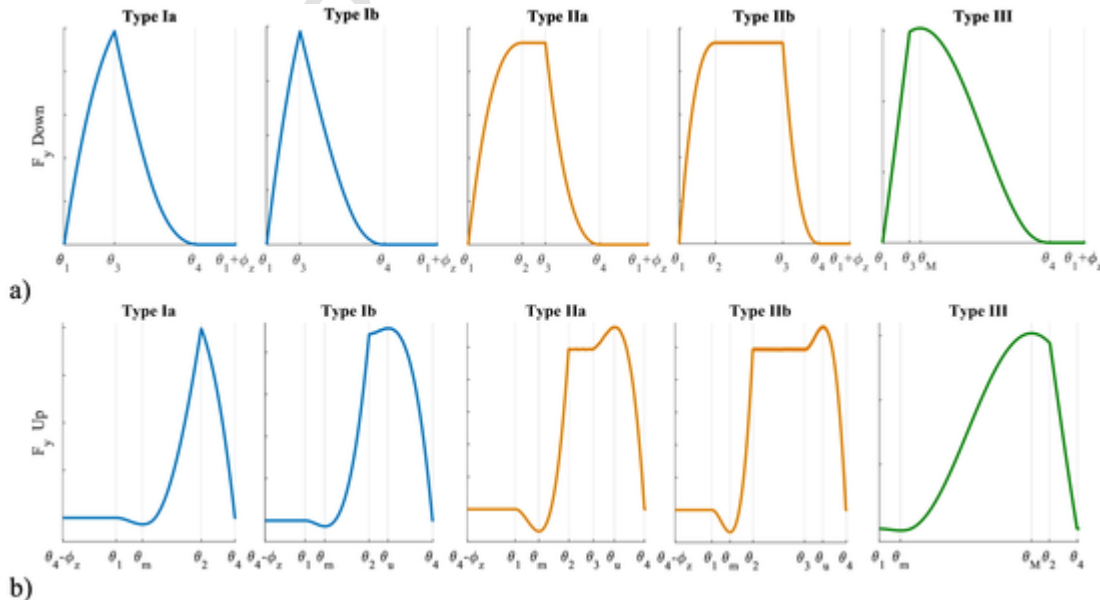


**Fig. 5.** Examples of single flute  $F_y$  shapes in one period a) Down-milling ( $\theta_1$ ;  $\theta_1 + \phi_z$ ) b) Up-milling ( $\theta_4 - \phi_z$ ;  $\theta_4$ ).

**Table 2**  
Single flute  $F_y$  profile key angles.

	Ia	Ib	IIa	IIb	III
Down-milling	$\vartheta_1, \vartheta_3, \vartheta_4$	$\vartheta_1, \vartheta_3, \vartheta_4$	$\vartheta_1, \vartheta_2, \vartheta_3, \vartheta_4$	$\vartheta_1, \vartheta_2, \vartheta_3, \vartheta_4$	$\vartheta_1, \vartheta_3, \vartheta_M, \vartheta_4$
Up-milling	$\vartheta_1, \vartheta_m, \vartheta_2, \vartheta_4$	$\vartheta_1, \vartheta_m, \vartheta_2, \vartheta_u, \vartheta_4$	$\vartheta_1, \vartheta_m, \vartheta_2, \vartheta_3, \vartheta_u, \vartheta_4$	$\vartheta_1, \vartheta_m, \vartheta_2, \vartheta_3, \vartheta_u, \vartheta_4$	$\vartheta_1, \vartheta_m, \vartheta_M, \vartheta_2, \vartheta_4$

$F_y$  shape, and, at the same time, the constant portion of the previous single flute  $F_y$  shape influences the constant portion of the following single flute  $F_y$  shape.

- Deep high overlap (h): This configuration applies to both type IIb and type IIa. In detail, this condition occurs when the rising edge of the previous single flute  $F_y$  shape influences the rising edge of the following single flute  $F_y$  shape, and, at the same time, the constant portion of the previous single flute  $F_y$  shape influences the constant portion of the following single flute  $F_y$  shape.

From an analytical point of view, the amount of overlap is strictly related to the tool pitch angle  $\phi_z$  which determines the reciprocal position between two consecutive single flute  $F_y$  shapes. Considering the pitch angle ( $\phi_z$ ), the number of flutes involved in the cut ( $n$ ) was defined as follows:

$$n \sim \frac{\alpha_{sw} + \alpha_{en}}{\phi_z} + 1 \quad (22)$$

where  $\sim$  indicates the rounding to the nearest integer towards minus infinity.

Depending on the engagement angles ( $\alpha_{en}$  and  $\alpha_{sw}$ ), the critical radial engagement angle ( $\alpha_{enc}$ ) and the pitch angle ( $\phi_z$ ), the analytical equations, which identify the degree of overlap for each single flute  $F_y$  shape in both down-milling and up-milling, are summarized in Table 3. This classification allows the identification of different multiple flutes  $F_y$  shapes for each type of single flute  $F_y$  shape/degree of overlap combination. Moreover, the type and the degree of overlap are related to few

factors ( $\alpha_{en}$ ,  $\alpha_{sw}$ ,  $\alpha_{enc}$ ,  $\phi_z$ ) which can be analytically obtained from the cutting parameters ( $ar$ ,  $ap$ ) and the tool geometry ( $D$ ,  $\alpha_{el}$ ,  $N$ ).

However, in the medium and high overlap configurations, with the same type/degree of overlap, the number of flutes involved in the cut ( $n$ ) may significantly alter the multiple flute  $F_y$  shape. Indeed, when  $n$  single flute  $F_y$  shapes overlap one another, it is tricky to identify which key angle of which single flute  $F_y$  shape is relevant for the resultant multiple flutes  $F_y$  shape. In such conditions, the multiple flute  $F_y$  shape evolve in a limited range, and the number of flutes axially involved in the cut ( $v$ ) becomes relevant. Therefore, starting from the key angles defined for a single fluted endmill, the additional key angles relevant for the resultant multiple flute  $F_y$  shape are defined as follows for down-milling and up-milling:

$$\vartheta_{px} = \vartheta_x - v\phi_z \quad x = 1, 2, 3, M, 4 \quad (\text{down - milling}) \quad (23)$$

$$\vartheta_{fx} = \vartheta_x + v\phi_z \quad x = 1, m, 2, 3, u, M, 4 \quad (\text{up - milling}) \quad (24)$$

$$v \sim \alpha_{sw}/\phi_z \quad (25)$$

Despite the increased number of key angles, as the cutting conditions ( $ar$ ,  $ap$ ) changes, the slope of the rising/falling edges of the single flute  $F_y$  shapes change, and, depending on the number of flutes involved ( $n$  and  $v$ ), some of the key angles defined may not contribute to the multiple flute  $F_y$  shape. Thus, the cutting conditions, which allow a specific key angle to be relevant for the multiple flute  $F_y$  shape in a specific type/degree of overlap configuration, are expressed with a series of Eqs. (26)–(33).

$$\alpha_{sw} + \alpha_{en} < 2\phi_z \quad (26)$$

$$\alpha_{sw} + \alpha_{en} < (v+1)\phi_z \quad (27)$$

$$\exists i \in (0, 1, \dots, n) : \alpha_{en} + \alpha_{sw} - \phi_z < \vartheta_2 + i\phi_z < \alpha_{sw} \quad (\text{down - milling}) \quad (28)$$

$$\alpha_{en} + \alpha_{sw} - \phi_z < \alpha_{enu} - \alpha_{sw} \quad (\text{up - milling}) \quad (29)$$

$$\alpha_{en} + \alpha_{sw} - \phi_z < 2\phi_z + \alpha_{enu} - \alpha_{sw} \quad (\text{up - milling}) \quad (30)$$

$$\alpha_{en} + \alpha_{sw} - \phi_z < (v+1)\phi_z + \alpha_{enu} - \alpha_{sw} \quad (\text{up - milling}) \quad (31)$$

$$\exists i \in (0, 1, \dots, n) : \alpha_{en} < \vartheta_3 - i\phi_z < \phi_z \quad (\text{up - milling}) \quad (32)$$

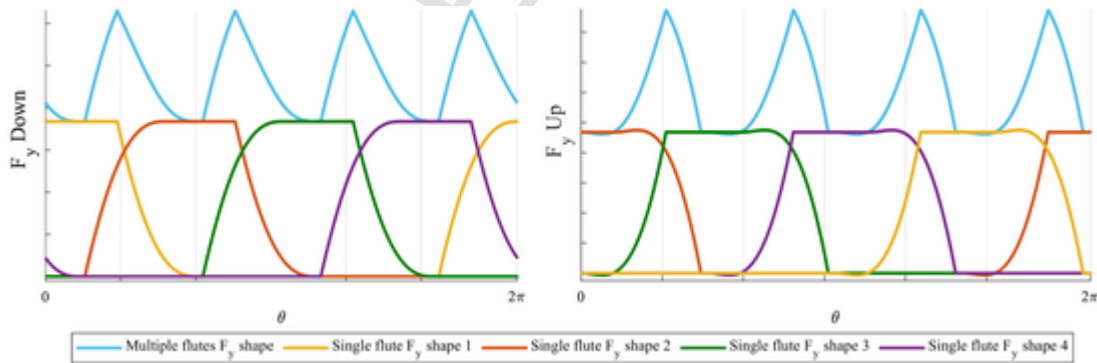


Fig. 6. Example of multiple flutes endmill  $F_y$  shape for both down-milling and up-milling.

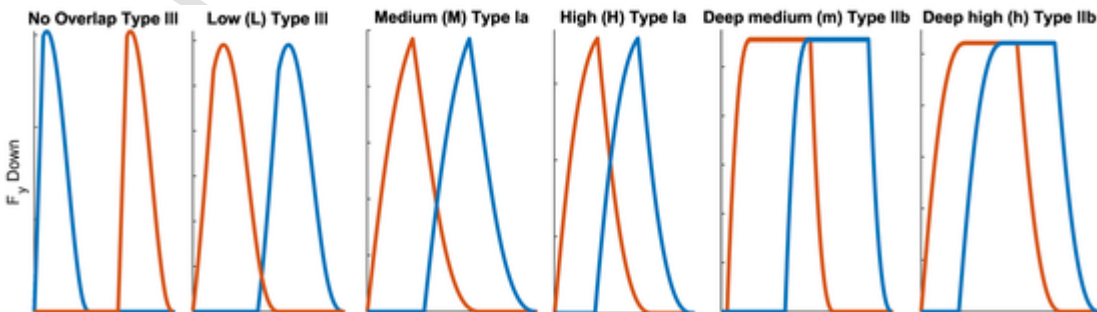


Fig. 7. Examples of different degrees of overlap for different types of single flute  $F_y$  shape in down-milling.

**Table 3**  
Overlap degrees for both down-milling and up-milling.

	No overlap	Low overlap (L)	Medium overlap (M)	High overlap (H)	Deep medium overlap (m)	Deep high overlap (h)
Type Ia/Type Ib	$\alpha_{en} + \alpha_{sw} < \phi_z$	$\alpha_{en} + \alpha_{sw} \geq \phi_z$ $\alpha_{en} < \phi_z$ $\alpha_{sw} < \phi_z$	$\alpha_{en} + \alpha_{sw} \geq \phi_z$ $\alpha_{en} \geq \phi_z$ $\alpha_{sw} < \phi_z$	$\alpha_{en} + \alpha_{sw} \geq \phi_z$ $\alpha_{en} \geq \phi_z$ $\alpha_{sw} \geq \phi_z$	n/a	n/a
Type IIa	$\alpha_{en} + \alpha_{sw} < \phi_z$	$\alpha_{en} + \alpha_{sw} \geq \phi_z$ $\alpha_{en} < \phi_z$ $\alpha_{sw} < \phi_z$	$\alpha_{en} + \alpha_{sw} \geq \phi_z$ $\alpha_{en} < \phi_z$ $\alpha_{sw} \geq \phi_z$ $\alpha_{sw} < \phi_z + \alpha_{en}$	$\alpha_{en} + \alpha_{sw} \geq \phi_z$ $\alpha_{en} \geq \phi_z$ $\alpha_{sw} \geq \phi_z$ $\alpha_{sw} < \phi_z + \alpha_{en}$	n/a	$\alpha_{en} + \alpha_{sw} \geq \phi_z$ $\alpha_{en} \geq \phi_z$ $\alpha_{sw} \geq \phi_z$ $\alpha_{sw} \geq \phi_z + \alpha_{en}$
Type IIb	$\alpha_{en} + \alpha_{sw} < \phi_z$	$\alpha_{en} + \alpha_{sw} \geq \phi_z$ $\alpha_{en} < \phi_z$ $\alpha_{sw} < \phi_z$	$\alpha_{en} + \alpha_{sw} \geq \phi_z$ $\alpha_{en} < \phi_z$ $\alpha_{sw} \geq \phi_z$ $\alpha_{sw} < \phi_z + \alpha_{en}$	n/a	$\alpha_{en} + \alpha_{sw} \geq \phi_z$ $\alpha_{en} < \phi_z$ $\alpha_{sw} \geq \phi_z$ $\alpha_{sw} \geq \phi_z + \alpha_{en}$	$\alpha_{en} + \alpha_{sw} \geq \phi_z$ $\alpha_{en} \geq \phi_z$ $\alpha_{sw} \geq \phi_z$ $\alpha_{sw} \geq \phi_z + \alpha_{en}$
Type III	$\alpha_{en} + \alpha_{sw} < \phi_z$	$\alpha_{en} + \alpha_{sw} \geq \phi_z$ $\alpha_{enc} < \phi_z$ $\alpha_{sw} + \alpha_{en} - \alpha_{enc} < \phi_z$	$\alpha_{en} + \alpha_{sw} \geq \phi_z$ $\alpha_{enc} \geq \phi_z$ $\alpha_{sw} + \alpha_{en} - \alpha_{enc} < \phi_z$	$\alpha_{en} + \alpha_{sw} \geq \phi_z$ $\alpha_{enc} \geq \phi_z$ $\alpha_{sw} + \alpha_{en} - \alpha_{enc} \geq \phi_z$	n/a	n/a

$$\exists i \in (0, 1, \dots, n) : \alpha_{en} < \vartheta_u - i\phi_z < \phi_z \text{ (up - milling)} \quad (33)$$

The Eqs. (26) and (27) apply to both down-milling and up-milling, while the others apply to either down-milling (28) or up-milling (29-30-31-32-33). Moreover, in up-milling, a higher number of equations is presented because the key angles describing  $F_y$  shape are more numerous and more sensitive to the cutting conditions. Considering the cutting conditions and the type/degree of overlap combination, the key angles identifying the multiple flutes  $F_y$  shape in one period (from  $\vartheta_1$  to  $\vartheta_1 + \phi_z$  in down-milling and from  $\vartheta_4 - \phi_z$  to  $\vartheta_4$  in up-milling) are summarized in Table 4 (down-milling) and Table 5 (up-milling). Each table also highlights the key angles which must satisfy one or another of the equations previously mentioned to affect the multiple flutes  $F_y$  shape.

In down-milling, for type Ia and Ib single flute  $F_y$  shapes, the identification of the key angles is straightforward in any configuration because no specific cutting condition affects the multiple flutes  $F_y$  shape. On the other hand, for type IIa and type IIb single flute  $F_y$  shapes, in the medium and deep medium overlap configurations, some of the key angles must verify certain cutting conditions to affect the multiple flutes  $F_y$  shape. Instead, for type III the key angles identification is straightforward as type Ia and type Ib.

In up-milling, the identification of the key angles is generally more complex compared to down-milling. Indeed, for each type of single flute  $F_y$  shape, some of the key angles are affected by the cutting conditions in at least one configuration. As an example, type IIb single flute  $F_y$  shape in deep medium overlap configurations shows several key angles, and most of them must satisfy different cutting conditions to impact on the multiple flute  $F_y$  shape. Moreover, it is interesting to note that, independently from the type of single flute  $F_y$  shape and the cut-

**Table 4**  
Multiple  $F_y$  shape key angles for one period ( $\vartheta_1$ ;  $\vartheta_1 + \phi_z$ ) in down-milling.

	Type Ia	Type Ib	Type IIa	Type IIb	Type III
No overlap	$\vartheta_1, \vartheta_3, \vartheta_4$	$\vartheta_1, \vartheta_3, \vartheta_4$	$\vartheta_1, \vartheta_2, \vartheta_3, \vartheta_4$	$\vartheta_1, \vartheta_2, \vartheta_3, \vartheta_4$	$\vartheta_1, \vartheta_3, \vartheta_M, \vartheta_4$
Low (L)	$\vartheta_1, \vartheta_3$	$\vartheta_1, \vartheta_3$	$\vartheta_1, \vartheta_2, \vartheta_3$	$\vartheta_1, \vartheta_2, \vartheta_3$	$\vartheta_1, \vartheta_3, \vartheta_M$
Medium (M)	$\vartheta_1, \vartheta_3$	$\vartheta_1, \vartheta_3$	$\vartheta_1, \vartheta_{p3}, \vartheta_{p4}$ if (26)	$\vartheta_1, \vartheta_{p3}, \vartheta_{p4}$ if (26)	$\vartheta_1, \vartheta_3$
High (H)	$\vartheta_1, \vartheta_{p3}$	$\vartheta_1, \vartheta_{p3}$	$\vartheta_1, \vartheta_{p3}$	n/a	$\vartheta_1, \vartheta_{p3}$
Deep medium (m)	n/a	n/a	n/a	$\vartheta_1, \vartheta_{p3}, \vartheta_2$ if (28) $\vartheta_{p4}$ if (27)	n/a
Deep high (h)	n/a	n/a	$\vartheta_1, \vartheta_{p3}$	$\vartheta_1, \vartheta_{p3}$	n/a

**Table 5**  
Multiple  $F_y$  shape key angles for one period ( $\vartheta_4 - \phi_z$ ;  $\vartheta_4$ ) in up-milling.

	Type Ia	Type Ib	Type IIa	Type IIb	Type III
No overlap	$\vartheta_1, \vartheta_m, \vartheta_2, \vartheta_4$	$\vartheta_1, \vartheta_m, \vartheta_2, \vartheta_u, \vartheta_4$	$\vartheta_1, \vartheta_m, \vartheta_2, \vartheta_3, \vartheta_u, \vartheta_4$	$\vartheta_1, \vartheta_m, \vartheta_2, \vartheta_3, \vartheta_u, \vartheta_4$	$\vartheta_1, \vartheta_m, \vartheta_M, \vartheta_2, \vartheta_4$
Low (L)	$\vartheta_2, \vartheta_4$ $\vartheta_m$ if (29)	$\vartheta_2, \vartheta_u, \vartheta_4$ $\vartheta_m$ if (29)	$\vartheta_2, \vartheta_3, \vartheta_u, \vartheta_4$ $\vartheta_m$ if (29)	$\vartheta_2, \vartheta_3, \vartheta_u, \vartheta_4$ $\vartheta_m$ if (29)	$\vartheta_M, \vartheta_2, \vartheta_4$ $\vartheta_m$ if (29)
Medium (M)	$\vartheta_2, \vartheta_4$	$\vartheta_2, \vartheta_4$	$\vartheta_{f2}, \vartheta_4$ $\vartheta_{f1}$ if (26) $\vartheta_{fm}$ if (30)	$\vartheta_{f2}, \vartheta_4$ $\vartheta_{f1}$ if (26) $\vartheta_{fm}$ if (30) $\vartheta_u$ if (33)	$\vartheta_2, \vartheta_4$
High (H)	$\vartheta_{f2}, \vartheta_4$	$\vartheta_{f2}, \vartheta_4$	$\vartheta_{f2}, \vartheta_4$	n/a	$\vartheta_2, \vartheta_4$
Deep medium (m)	n/a	n/a	n/a	$\vartheta_{f2}, \vartheta_4$ $\vartheta_{f1}$ if (27) $\vartheta_{fm}$ if (31) $\vartheta_3$ if (32) $\vartheta_u$ if (33)	n/a
Deep high (h)	n/a	n/a	$\vartheta_{f2}, \vartheta_4$	$\vartheta_{f2}, \vartheta_4$	n/a

ting strategy, in the high and deep high overlap configurations very few key angles identify the multiple flutes  $F_y$  shape because, in such configurations, the amplitude of one period is extremely small, and few key angles fall into such a small range.

### 3.3. Key points axial position

In the previous sections the key angles describing the  $F_y$  shape in one period, for both a single fluted endmill (3.1) and a multiple fluted endmill (3.2), were defined. In this section, such key angles are first selected to describe the shape of surface generating force in the engagement angle domain  $\vartheta$ . Then, the key angles selected are used to obtain the axial position of the key points characterizing the surface error shape through dedicated equations.

### 3.4. Surface generating force

Focusing on the first step, the shape of the surface generating force is represented by the portion of  $F_y$  contained in the surface generation range (2). Therefore, by selecting the key angles, which describe the  $F_y$  shape within the surface generation range, the shape of the surface generating force is obtained. In detail, the selection of these key angles is



strictly related to both the cutting strategy and the number of flutes involved in the cut  $n$ .

In down-milling, the surface generation range is expressed by Eq. (3) therefore, considering the key angles previously expressed (3.1), the boundaries of the surface generating force are identified by the key angles  $\vartheta_2$  (starting angle) and  $\vartheta_4$  (ending angle). In up-milling, instead, the surface generation range is expressed by Eq. (4) therefore the boundaries of the surface generating force are identified by the key angles:  $\vartheta_1$  (starting angle) and  $\vartheta_3$  (ending angle). Between the starting and ending angle, the key angles describing the surface generating force shape are selected from the key angles defining  $n$  periods of the  $F_y$  shape. In detail, taking as reference the key angles previously described (3.1, 3.2) for the starting period, the key angles of the other  $n-1$  periods are obtained as follows:

$$\begin{aligned} \vartheta_{id}^k &= \vartheta_{id}^1 + (k-1)\phi_z k \\ &= 1, 2, \dots, n-1 \text{ (down - milling)} \end{aligned} \quad (34)$$

$$\begin{aligned} \vartheta_{iu}^k &= \vartheta_{iu}^1 - (k-1)\phi_z k \\ &= 1, 2, \dots, n-1 \text{ (up - milling)} \end{aligned} \quad (35)$$

In down-milling,  $\vartheta_{id}^1$  is the generic key angle defined in the starting period while  $\vartheta_{id}^k$  represents the same key angle defined in the  $k$ -th period following the starting one. In up-milling, instead,  $\vartheta_{iu}^1$  is the generic key angle defined in the starting period while  $\vartheta_{iu}^k$  represents the same key angle defined in the  $k$ -th period preceding the starting one. At this point, the key angles defining the surface generating force shape are the ones, selected from the  $n$  periods considered, which fall into the interval

between the starting angle and the ending angle, as it is exemplified in Fig. 8 for down-milling and in Fig. 9 for up-milling.

#### 3.4.1. Surface error

In the second part of this section, the key angles, which describe the surface generating force shape are used to investigate the surface error shape. Indeed, each key angle represents not only a key point of the surface generating force but also an axial position assumed by the flute during the surface generation process (Fig. 2). Therefore, considering the tool geometry and the starting angle of the surface generation process, the axial positions of the key points describing the surface error shape are obtained with the following equations:

$$\begin{aligned} z_{sdj} &= (\vartheta_{sdj} - \phi_{out}) / k_b j \\ &= 1, 2, \dots, q \text{ (down - milling)} \end{aligned} \quad (36)$$

$$z_{suj} = (\vartheta_{suj} - \phi_{in}) / k_b j = 1, 2, \dots, q \text{ (up - milling)} \quad (37)$$

In down-milling,  $\vartheta_{sdj}$  is the generic key angle characterizing the surface generating force shape, and  $z_{sdj}$  is the axial position corresponding  $\vartheta_{sdj}$ . On the other hand, in up-milling,  $\vartheta_{suj}$  is the generic key angle characterizing the surface generating force shape, and  $z_{suj}$  is the axial position corresponding  $\vartheta_{suj}$ . In both cases,  $q$  represents the number of key angles characterizing the surface generating force shape. Taking the surface generating force shapes from the previous examples (Figs. 8, 9), an example of key points axial position evaluation for both down-milling and up-milling is presented in Fig. 10.

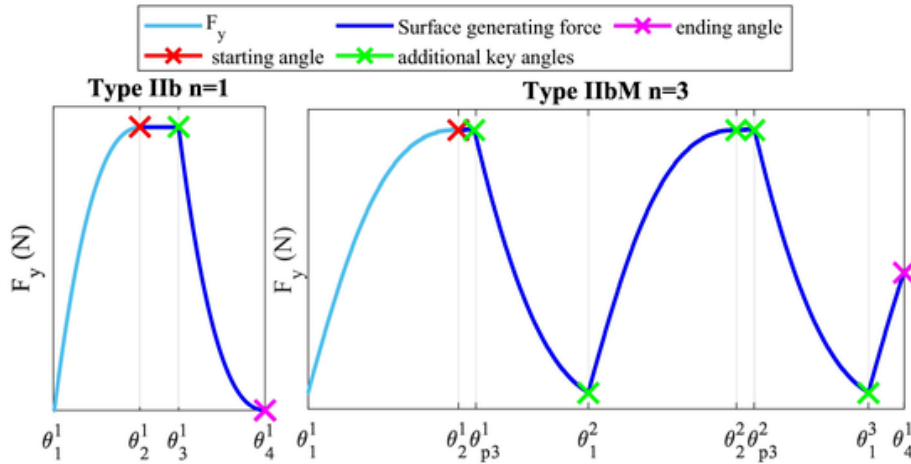


Fig. 8. Examples of key angles selection for the surface generating force in down-milling ( $n = 1$  and  $n = 3$ ).

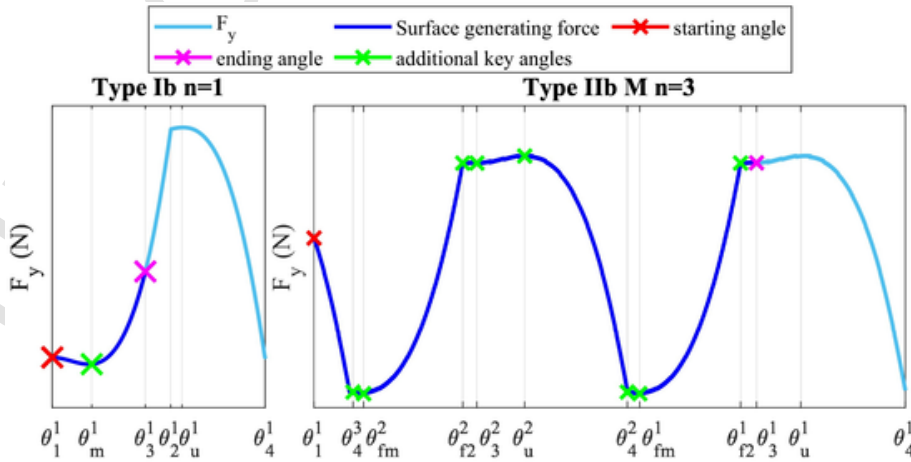


Fig. 9. Examples of key angles selection for the surface generating force in up-milling ( $n = 1$  and  $n = 3$ ).

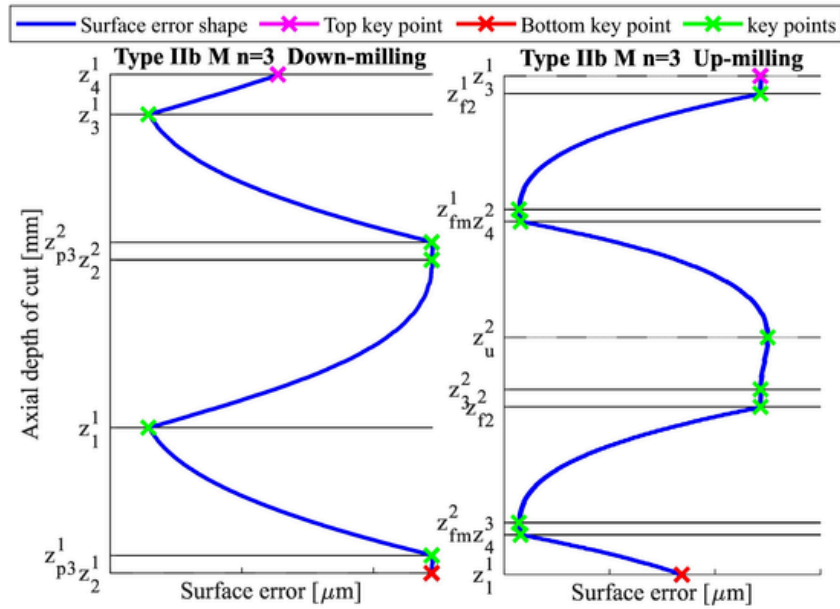


Fig. 10. Examples of key points axial positions evaluation in Down-milling and Up-milling.

#### 4. Experimental validation

The proposed approach was experimentally validated through several milling tests so that different types with different degrees of overlap are examined. In each test, both cutting forces and the machined surface were measured to obtain the  $F_y$  shape and the surface error shape. First, the setup for the milling tests is presented including force and surface acquisition methods. Then, for each test, the experimental  $F_y$  shape and the measured surface error shape are compared with the analytical results of the proposed approach. Finally, the presented approach is applied to a surface error prediction method.

##### 4.1. Set-up

The milling tests were conducted on a DMG MORI DMU 75 MONOBLOCK machine tool with two different endmills, (Garant 202552) and (Garant 202274), depending on the feasibility of the type-

degree of overlap combination. The geometrical features and the fixed cutting parameters of each tool are summarized in Table 6.

A stiff workpiece (50x80x90mm) made of aluminium (6082-T4) was adopted to perform the cutting tests. In detail, the workpiece was prepared to include at least two milling tests (one in down-milling and one in up-milling) at a time (Fig. 11a). Each time the surface was machined, it was flattened and prepared again for the following tests. For these two tool/workpiece couples the cutting force coefficients presented in Table 7 were adopted. The coefficients were experimentally identified by preliminary testing in slotting conditions and using the average force method as presented by Altintas [28]. Even though average measured forces were adopted, the obtained cutting coefficients are suitable to analyze  $F_y$  at any angular position as it is shown in [29].

As far as force measurements are concerned, the workpiece was clamped to a Kistler 9257A table dynamometer which was mounted on the rotating table of the machine tool (Fig. 11b). Regarding the surface error, the on-machine measuring probe (RENISHAW Power Probe 60) was used to acquire the surface before and after each test (Fig. 11c). The type-degree of overlap combination and the corresponding cutting parameters including the endmill adopted for every cutting test are reported in Table 8. It must be noted that the high and deep high overlap configurations were not tested because they require several flutes cutting simultaneously and aggressive cutting parameters, configurations that rarely occur.

Table 6

Endmill parameters.

Endmill	Tool ID	D (mm)	N	$\alpha_{el}$ (deg)	Cutting length (mm)	$f_z$ (mm/flute)	Spindle Speed (rpm)
202,552	1	12	4	45	36	0.1	6366
202,274	2	10	3	45	16	0.04	12,732

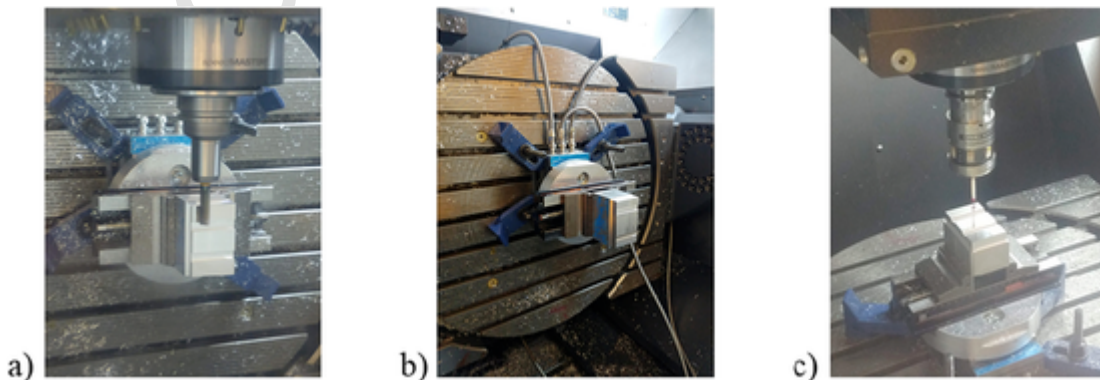


Fig. 11. Experimental set-up: a) milling test b) force measurement c) surface acquisition.

**Table 7**  
Cutting coefficients.

$K_{tc}$ (N/mm <sup>2</sup> )	$K_{rc}$ (N/mm <sup>2</sup> )
752.9	200.5

**Table 8**  
Milling tests overview.

Test	Type	Overlap	Strategy	Tool ID	ar (mm)	ap (mm)
1	Ia	No overlap	Down	1	2	3
2	Ia	Low	Down	1	3	4
3	Ia	Medium	Down	1	6	5
4	Ia	Medium	Down	1	6.5	5
5	Ia	No overlap	Up	1	2	3
6	Ia	Low	Up	1	3	4
7	Ia	Medium	Up	1	6	5
8	Ia	Medium	Up	1	6.5	5
9	Ib	No overlap	Down	2	3	2
10	Ib	Low	Down	2	5	3
11	Ib	Medium	Down	1	6	3
12	Ib	Medium	Down	1	6.5	3
13	Ib	No overlap	Up	2	2.5	4
14	Ib	Low	Up	2	3	5
15	Ib	Medium	Up	1	6	8
16	Ib	Medium	Up	1	6.5	8.5
17	IIa	No overlap	Down	1	1	5
18	IIa	Low	Down	1	1	7
19	IIa	Medium	Down	1	4	12.4
20	IIa	No overlap	Up	1	1	5
21	IIa	Low	Up	1	1	7
22	IIa	Medium	Up	1	4	12.4
23	IIb	No overlap	Down	1	0.6	5.5
24	IIb	Low	Down	1	1	8
25	IIb	Medium	Down	1	2.5	12
26	IIb	Deep medium	Down	1	2	20
27	IIb	No overlap	Up	1	0.6	5.5
28	IIb	Low	Up	1	1	8
29	IIb	Medium	Up	1	2.5	12
30	IIb	Deep medium	Up	1	2	18
31	III	No overlap	Down	2	6	1
32	III	Low	Down	1	6	1
33	III	Medium	Down	1	7.5	2.5
34	III	No overlap	Up	2	6.5	1
35	III	Low	Up	2	7	2
36	III	Medium	Up	2	8	4

## 4.2. Force shape

The cutting forces were measured, compensated to reduce the impact of the system dynamic on the cutting force measurements [30] and post-processed to reduce measurement noise and compensate tool run-out as in [29]. This compensation allows the clear identification of the force shape in one period. The obtained cutting forces are shown in groups based on the type of single flute single flute  $F_y$  shape (Fig. 13, Fig. 14, Fig. 15, Fig. 16, Fig. 17). In each chart the vertical axis represents the unity based normalized  $F_y$  magnitude  $F^*$ , and the horizontal axis reports the engagement angle range  $\vartheta^*$  corresponding to one period of  $F_y$  normalized by the tool pitch angle. In detail, the engagement angle range is limited from  $\vartheta_1$  to  $\vartheta_1 + \phi_z$  in down-milling and from  $\vartheta_4 - \phi_z$  to  $\vartheta_4$  in up-milling. The equations to derive  $F^*$  and  $\vartheta^*$  are provided below:

$$F^* = \frac{F_{yk} - \min(F_y)}{\max(F_y) - \min(F_y)} \quad (38)$$

where  $F_{yk}$  is the generic  $k$  value of  $F_y$  in one period, while  $\max(F_y)$  and  $\min(F_y)$  represent the maximum and minimum values of  $F_y$  in one period.

$$\vartheta^* = \frac{\vartheta_k - \vartheta_s}{\phi_z} \quad (39)$$

where  $\vartheta_k$  is the generic  $k$  value of the engagement angle in one period (from  $\vartheta_1$  to  $\vartheta_1 + \phi_z$  in down-milling and from  $\vartheta_4 - \phi_z$  to  $\vartheta_4$  in up-milling), while  $\vartheta_s$  is the starting angle equal to  $\vartheta_1$  in down-milling and  $\vartheta_4 - \phi_z$  in up-milling. Examples of comparison between measured forces and normalized forces for tests 1 and 4 are provided in Fig. 12.

In the following figures the force shapes of the different tests are analyzed. Each chart reports one period of  $F_y$  (blue) and the analytical key angles (red lines) obtained to verify the reliability of the proposed approach.

Fig. 13 presents the  $F_y$  shapes for type Ia with three different degrees of overlap, no overlap, low (L) and medium (M) for both down-milling (first row) and up-milling (second row). With no overlap, only one flute is involved in the cut, thus the  $F_y$  shape in one period is composed by the single flute  $F_y$  shape and a constant portion representing the absence of cut in both down-milling (test 1) and up-milling (test 5). Indeed, good agreement is shown between the measured  $F_y$  shape and the proposed key angles for both cutting strategies. In detail, in up-milling,  $F_y$  shape presents a valley with a minimum identified by the key angle  $\vartheta_m$ , but, due to the low radial and axial depths of cut characterizing the type Ia in the no overlap configuration, this valley is

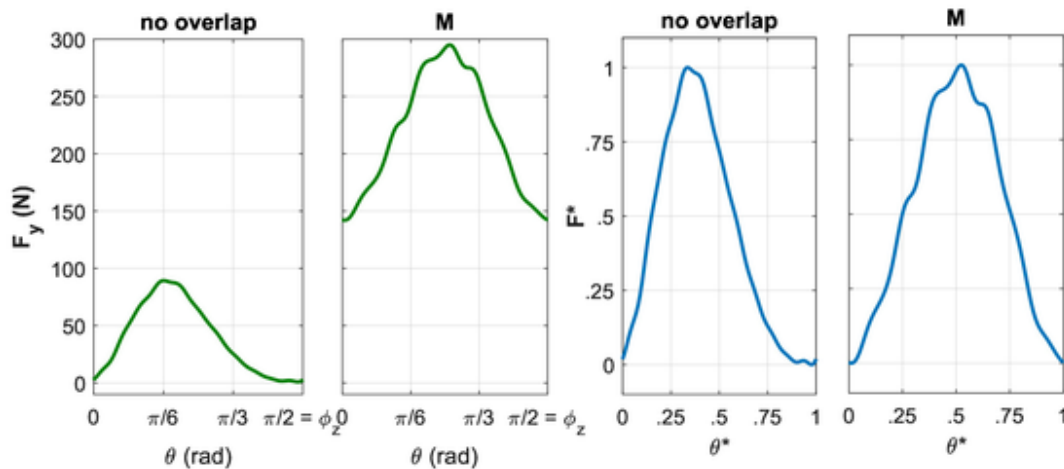


**Fig. 12.** Example of normalized force and engagement angle range (right) compared to the actual measured force (left) for test 1 and 4.

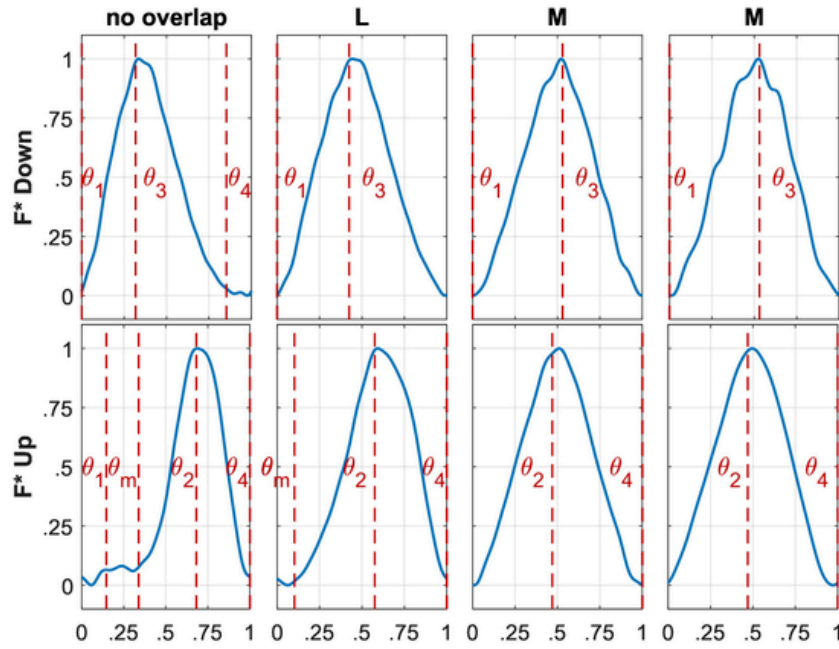


Fig. 13. Type Ia normalized  $F_y$  shapes (tests 1 to 4 in down-milling; tests 5 to 8 in up-milling).

poorly highlighted in the measured  $F_y$  shape. As both radial and axial depths of cut increase, another flute joins the cut, thus the constant portion disappears, and low overlap occurs. Indeed, for down-milling (test 2), as soon as a second flute joins the cut, the high cutter exit angle ( $\vartheta_4$ ) is deleted by the rising edge of the second single flute  $F_y$  shape involved in the cut. Therefore, the  $F_y$  period is reduced, and its shape is identified by a smaller number of key angles, the low cutter entry angle ( $\vartheta_1$ ) and the high cutter entry angle ( $\vartheta_3$ ) in agreement with the experimental result. Instead, for up-milling (test 6), as soon as a second flute joins the cut, the low cutter entry angle ( $\vartheta_1$ ) is deleted by the falling edge of the second single flute  $F_y$  shape involved in the cut. Thus, the  $F_y$  shape is identified by the minimum angle ( $\vartheta_m$ ), the low cutter exit angle ( $\vartheta_2$ ) and the high cutter exit angle ( $\vartheta_4$ ). The proposed key angles are in good match with the measured force, and, thanks to the higher depths adopted, the valley of the  $F_y$  shape, which is identified by  $\vartheta_m$ , is more highlighted in this case. Moreover, it must be noted that this valley appears in the  $F_y$  shape only because the cutting parameters adopted do not allow the falling edge of the second single flute  $F_y$  shape to delete it. This concept is expressed by Eq. (29), which is verified for test 6. With more aggressive cutting parameters the amount of overlap between the two single flute  $F_y$  shapes increases, and medium overlap is obtained. In this configuration the amplitude of  $F_y$  period is considerably reduced limiting the variations of the force shape. Indeed, in down-milling (test 3 and test 4), the  $F_y$  shape is the same as in the low overlap configuration since no other key angle was deleted. On the other hand, in up-milling (test 7 and test 8), regardless the cutting parameters adopted  $\vartheta_m$  is not present in  $F_y$  shape because it is deleted by the second single flute  $F_y$  shape. In both cutting strategies, with medium overlap good match is found between the measured force shapes and the proposed key angles.

Fig. 14 shows the  $F_y$  shapes for type Ib in three different configurations, no overlap, low overlap (L) and medium overlap (M) for both down-milling (first row) and up-milling (second row). In down-milling, the proposed key angles fairly represent  $F_y$  shape in most of the configurations. Focusing on down-milling, type Ib differs from type Ia only for the magnitude of  $\alpha_{en}$  which changes the relative distance between  $\vartheta_1$  and  $\vartheta_3$ . Despite this difference, the same observations made for type Ia apply also to type Ib. On the other hand, in up-milling (test 13), type Ib is significantly different from type Ia due to the additional key angle ( $\vartheta_u$ ). In the no overlap configuration, only one flute is involved in the

cut, but, due to the low signal to noise ratio, the constant portion representing the absence of cut and the portion between  $\vartheta_1$  and  $\vartheta_m$  of the single flute  $F_y$  shape are altered, thus they are not clearly highlighted in the measured force. Moreover, due to the cutting parameters adopted for this configuration the distance between  $\vartheta_2$  and  $\vartheta_u$  is small. Nonetheless, this short distance allows the maximum of the measured  $F_y$  shape to be clearly identified according with the proposed formulations. As the cutting parameters increase, another flute joins the cut and low overlap is obtained (test 14). Analogously to type Ia, as soon as the second flute joins the cut the low cutter entry angle ( $\vartheta_1$ ) is deleted by the second single flute  $F_y$  shape. Moreover, in test 14, the key angle  $\vartheta_m$  is not considered for the  $F_y$  shape, as it is confirmed by the measured  $F_y$  shape. Indeed, due to the cutting parameters adopted, the second single flute  $F_y$  shape overlaps the single flute  $F_y$  shape of reference deleting  $\vartheta_m$ , as it is expressed by Eq. (29), which is not verified in this case. Furthermore, in this configuration, despite the small difference, the difference between  $\vartheta_2$  and  $\vartheta_u$  is better highlighted. Using higher depths of cut, the amount of overlap between the two single flute  $F_y$  shapes increases, and medium overlap is found (test 16). In this condition, the amplitude of the  $F_y$  period is heavily reduced limiting the variations of the  $F_y$  shape. Indeed, in this configuration, the measured  $F_y$  shape presents a triangular shape, which is significantly different from the corresponding single flute  $F_y$  shape. According to this different shape, the proposed approach gives two key angles  $\vartheta_2$  and  $\vartheta_4$ , which despite small deviations still identify the triangular shape. It must be noted that these small deviations appear overstated in the figure on account of the small amplitude of the  $F_y$  period. Moreover, despite the key angle  $\vartheta_u$  identifies the maximum of the single flute  $F_y$  shape, in the medium overlap configuration it does not affect the  $F_y$  shape because the effect of the rising edge of the second single flute  $F_y$  shape is dominant compared to the amplitude of the peak of the reference single flute  $F_y$  shape.

In Fig. 15 the  $F_y$  shapes for type IIa in three different configurations, no overlap, low overlap (L) and medium overlap (M) for both down-milling (first row) and up-milling (second row) are presented. In down-milling (test 17), for the no overlap configuration where only one flute is involved in the cut, both the constant portion and the trapezoidal shape of the type IIa single flute  $F_y$  shape are well identified by the proposed key angles. As the axial depth of cut increases, another flute joins the cut, low overlap is found (test 18), and the high cutter exit angle ( $\vartheta_4$ ) is deleted by the second single flute  $F_y$  shape. As both radial and ax-



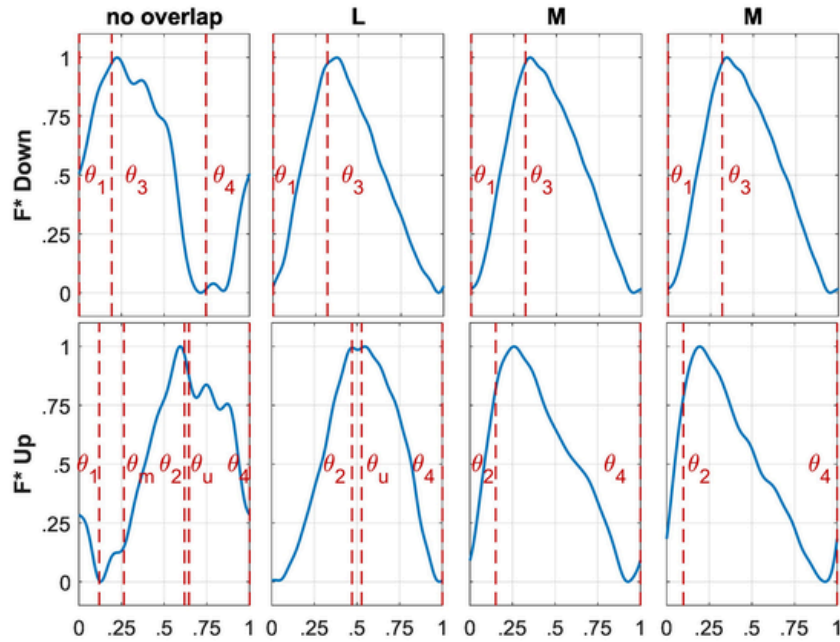


Fig. 14. Type Ib normalized  $F_y$  shapes (tests 9 to 12 in down-milling; tests 13 to 16 in up-milling).

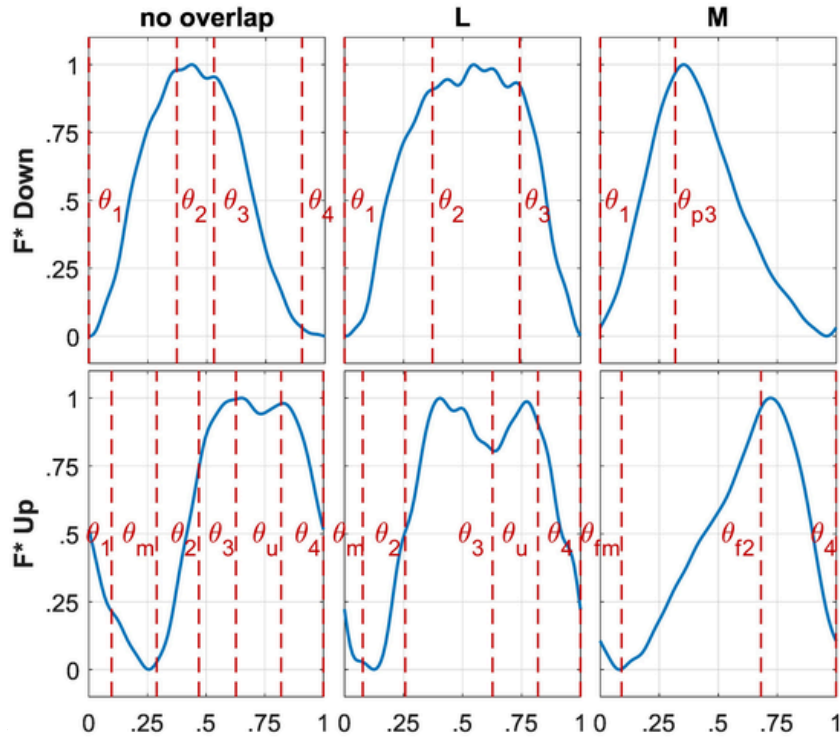


Fig. 15. Type IIa normalized  $F_y$  shapes (tests 17 to 19 in down-milling; tests 20 to 22 in up-milling).

ial depths of cut are increased, more flutes join the cut, the amount of overlap between two consecutive single flute  $F_y$  shapes becomes more significant, and medium overlap is obtained (test 19). In this case, due to the small amplitude of the  $F_y$  period the variations in the  $F_y$  shape are limited. Indeed, the measured  $F_y$  shape presents a simple triangular shape, which is significantly different from the corresponding single flute  $F_y$  shape. Moreover, due to aggressive cutting parameters requested for this type/degree of overlap combination, also the key angles belonging to the other single flute  $F_y$  shapes involved in the cut become relevant for the overall  $F_y$  shape identification. In detail, for

down-milling, the key angles belonging to the single flute  $F_y$  shapes preceding the one of reference are selected for the overall  $F_y$  shape ( $\theta_{p3}$ ). Following these aspects, the proposed key angles well identify the measured  $F_y$  shape. Regarding the up-milling strategy, for the no overlap configuration (test 20), the constant portion is not well highlighted in the measured  $F_y$  shape, due to small signal to noise ratio; however, the trapezoidal shape of the type IIa single flute  $F_y$  shape is well recognizable. In detail, the proposed key angles, despite small deviations, well represents the valley, the constant portion, and the peak of type IIa. As the axial depth of cut is increased low overlap is found (test 21), and the



low cutter entry angle ( $\theta_1$ ) is deleted by the second single flute  $F_y$  shape involved in the cut. Moreover, since Eq. (29) is verified, the valley is still present in the  $F_y$  shape, and it is well identified by  $\theta_m$ . In this case the measured force shape is well identified by the proposed key angles, despite small deviations in the constant portion between  $\theta_2$  and  $\theta_3$ . With higher axial and radial depths of cut, several flutes join the cut, the amount of overlap between two consecutive single flute  $F_y$  shapes becomes consistent reducing the  $F_y$  period and limiting variations in the  $F_y$  shape. Indeed, also in up-milling, for the medium overlap condition (test 22), the measured  $F_y$  shape presents a simpler triangular shape. Following the proposed method, due to aggressive cutting parameters requested for this type/degree of overlap combination, also the key angles belonging to the other single flute  $F_y$  shapes involved in the cut become relevant for the overall  $F_y$  shape. However, in up-milling, the key angles belonging to the single flute  $F_y$  shape following the one of reference are the ones considered for the overall  $F_y$  shape ( $\theta_{f2}$  and  $\theta_{fm}$ ). Furthermore, it must be noted that for type IIa the valley identified by  $\theta_{fm}$  may be relevant also in the medium overlap configurations, unlike type Ia and type Ib, because, depending on the cutting conditions, the constant portion of the trapezoidal shape of the considered type IIa single flute  $F_y$  shape may overlap with the valley of one of the following type IIa single flute  $F_y$  shapes involved in the cutting process. This possibility is represented by Eq. (30), which is verified for test 22, therefore  $\theta_{fm}$  becomes relevant for the overall  $F_y$  shape. Overall, good match is obtained between the measured  $F_y$  shape and the proposed key angles.

Fig. 16 shows the  $F_y$  shapes for type IIb in four different configurations, no overlap, low overlap (L) medium overlap (M) and deep medium overlap (m) for both down-milling (first row) and up-milling (second row). In down-milling, for the no overlap and low overlap configurations (test 23 and test 24) the same observations made for type IIa also apply to type IIb. In the medium overlap configuration, the  $F_y$  shape is slightly different. Indeed, with more aggressive depths of cut, several flutes join the cut, and the period of  $F_y$  is reduced. In this condition, the constant portion characterizing the trapezoidal type IIb single flute  $F_y$  shape plays a crucial role in the identification of the cutting force shape because, depending on the cutting conditions, some of the key angles describing the single flute  $F_y$  shapes involved in the cut may overlap with the constant portion of the single flute  $F_y$  shape of reference and become relevant for the overall  $F_y$  shape. As it

is shown in test 25, the measured  $F_y$  shape assumes a triangular shape followed by a small constant portion, but the proposed key angles still identify the overall force shape. Indeed, the key angle  $\theta_{p4}$  is related to the cutting conditions through Eq. (26), which is verified for cutting conditions adopted, therefore such key angle becomes relevant for the cutting force shape identification. On the contrary, in test 23, where Eq. (26) is not verified, the  $\theta_{p4}$  is not relevant for  $F_y$  shape, as it is confirmed by the measured force shape. With higher depths of cut, more flutes join the cut, the period of  $F_y$  is reduced even more, and the deep medium overlap is found. Nonetheless, the  $F_y$  shape is well identified by the same key angles despite small deviations, and the same observations made for the medium overlap apply to the deep medium overlap case (test 26). However, it must be pointed out that despite being the same key angles the actual values of these angles is different since the cutting conditions adopted in tests 25 and 26 are different and a different number of flutes is involved in the cut. Moving to up-milling, for the no overlap configuration (test 27), due to the small difference between the peak value and the minimum value in the measured force, the trapezoidal shape cannot be easily identified. However, the key angles  $\theta_2$ ,  $\theta_3$ ,  $\theta_u$  and  $\theta_4$  well identify the constant portion and the peak of the single flute  $F_y$  shape. Instead, the valley describing the single flute  $F_y$  shape is not well represented by  $\theta_m$ , on account of the low signal to noise ratio. As both the radial and axial depth of cut increases, another flute joins the cut, low overlap is found (test 28), and the high cutter exit angle ( $\theta_4$ ) is deleted by the second single flute  $F_y$  shape involved in the cut. Moreover, thanks to the higher cutting forces the trapezoidal shape is more recognizable, and despite small deviations the proposed key angles well identify the measured  $F_y$  shape. With more aggressive depths of cut, several flutes join the cut, the period of  $F_y$  is reduced and the medium overlap is found. In this configuration the same observation made in down-milling also apply to up-milling. Indeed, in test 29, the measured  $F_y$  shape is composed by a small valley followed by a triangular shape, but the proposed key angles well identify the overall force shape. In detail, the valley portion, which is not well highlighted on account of the small amplitude, is identified by  $\theta_{f1}$  and  $\theta_{fm}$ , and they both depend on the cutting conditions through Eq. (26) and Eq. (30) respectively. On the other hand, the triangular portion of the  $F_y$  shape is identified by  $\theta_{f2}$  and  $\theta_4$ , which are always relevant for this configuration independently from the cut-

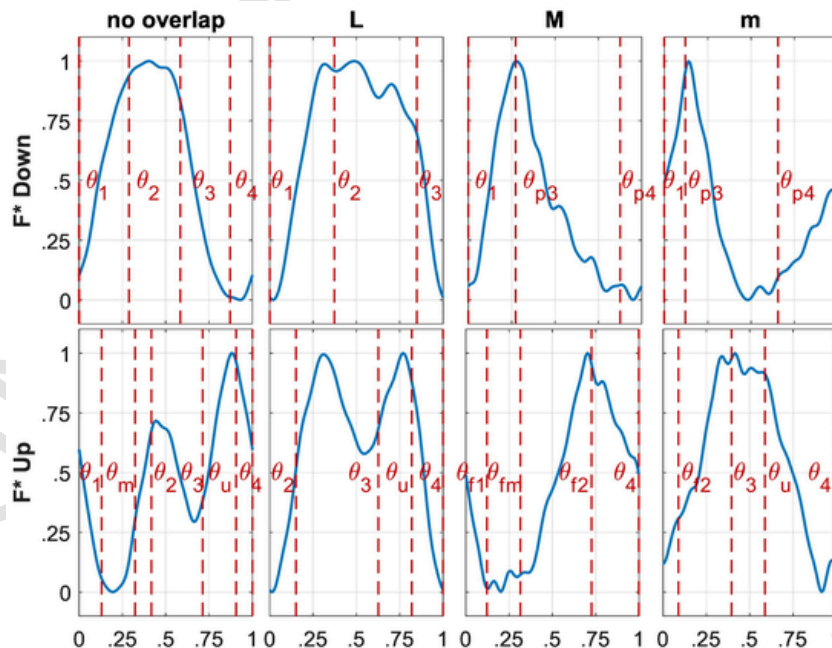


Fig. 16. Type IIb normalized  $F_y$  shapes (tests 23 to 26 in down-milling; tests 27 to 30 in up-milling).

ting conditions adopted. With higher axial depths of cut, more flutes join the cut, the period of  $F_y$  is reduced even more, and the deep medium overlap is found (test 30). In this case, the measured  $F_y$  shape is significantly different from the medium overlap configuration, but the proposed key angles well identify the trapezoidal shape assumed by the measured force. Moreover, in this case, cutting conditions still play a key role in the  $F_y$  shape identification. Indeed, the key angles  $\theta_{f2}$  and  $\theta_4$ , are still relevant like the previous case, but  $\theta_3$  and  $\theta_u$  are related to the cutting conditions through Eqs. (32) and (33) respectively. These equations are verified in test 30, therefore  $\theta_3$  and  $\theta_u$  are relevant for the  $F_y$  shape according with the measured  $F_y$  shape.

Fig. 17 presents the  $F_y$  shapes for type III in three different configurations, no overlap, low overlap (L) and medium overlap (M) for both down-milling (first row) and up-milling (second row). In down-milling, for the no overlap configuration (test 31), only one flute is involved in the cut, thus the  $F_y$  shape in one period is composed by the single flute  $F_y$  shape followed by constant portion representing the absence of cut. In test 31, due to the low signal to noise ratio, the measured  $F_y$  shape is significantly altered, and the proposed key angles do not clearly identify the features of the force shape. However, the proposed key angles still highlight the rising and the falling edge of the measured  $F_y$  shape. As soon as another flute joins the cut, low overlap is obtained (test 32), and high cutter exit angle ( $\theta_4$ ) is deleted by the second single flute  $F_y$  shape. In this case, the proposed key angles manage to identify the measured  $F_y$  shape. In detail, the peak is clearly highlighted since the high cutter entry angle ( $\theta_3$ ) and the peak angle ( $\theta_M$ ) are very close. Indeed, this short distance is related to the cutting parameters adopted which were imposed by type/degree overlap combination. However, due to this short distance, the difference between  $\theta_3$  and  $\theta_M$  cannot be seen in terms of force amplitude. As the depth of cut are increased, the amount of overlap between the two single flute  $F_y$  shapes increases and medium overlap is found (test 33). In this configuration, the peak angle ( $\theta_M$ ) is deleted by the rising edge of the second single flute  $F_y$  shape involved in the cut. Therefore, the  $F_y$  shape is identified only by  $\theta_1$  and  $\theta_3$ . However, the measured  $F_y$  shape presents a more complex evolution, which is the result of the rising/falling edges of the single flute  $F_y$  shapes overlapping one another. For this reason, a better identification cannot be obtained without adding

force simulation. In up-milling for the no overlap configuration (test 34) only one flute is involved in the cut, and the  $F_y$  shape in one period is composed by the single flute  $F_y$  shape followed by constant portion representing the absence of cut. In this case, the constant portion is almost absent due to the cutting parameters adopted. Nonetheless, the measured  $F_y$  shape well represents the type III single flute  $F_y$  shape according to the proposed key angles. In detail, it must be noted that due to cutting parameters adopted for the test, the peak angle ( $\theta_M$ ) and the low cutter exit angle are very close ( $\theta_2$ ). Therefore, the peak of the measured  $F_y$  shape is well highlighted, but the difference between  $\theta_2$  and  $\theta_M$  cannot be seen in terms of force amplitude. As the depths of cut are increased, another flute joins the cut, low overlap is obtained (test 32), and the low cutter entry angle ( $\theta_1$ ) is deleted by the second single flute  $F_y$  shape involved in the cut. Nonetheless, the proposed key angles identify the measured  $F_y$  shape. In detail, it must be noted that the valley identified by  $\theta_m$  affect the measured  $F_y$  shape because the cutting conditions adopted does not allow the second single flute  $F_y$  shape involved in the cut to delete this valley. This concept is represented by Eq. (29), which is verified for test 32, according with the measured  $F_y$  shape. As the depth of cut are increased, the amount of overlap between the two single flute  $F_y$  shapes increases and medium overlap is found (test 33). In this configuration, the peak angle ( $\theta_M$ ) is deleted by the falling edge of the second single flute  $F_y$  shape involved in the cut. Therefore, the  $F_y$  shape is identified only by  $\theta_2$  and  $\theta_4$ . However, the measured  $F_y$  shape presents a more complex evolution, which is the result of the rising/falling edges of the single flute  $F_y$  shapes overlapping one another. For this reason, a better identification cannot be obtained without adding force simulation.

#### 4.3. Surface error shape

Before each test, the initial workpiece surface was finished and measured. Then, after each cut, the newly machined surface was acquired, and the measured surface error profile was computed as the difference between the two acquired surfaces and the radial depth of cut. The measured surface error is affected by the tool runout since its impact cannot be compensated. However, following an indirect approach as in [31], tool runout was measured for both tools (0.006 mm for tool 1,

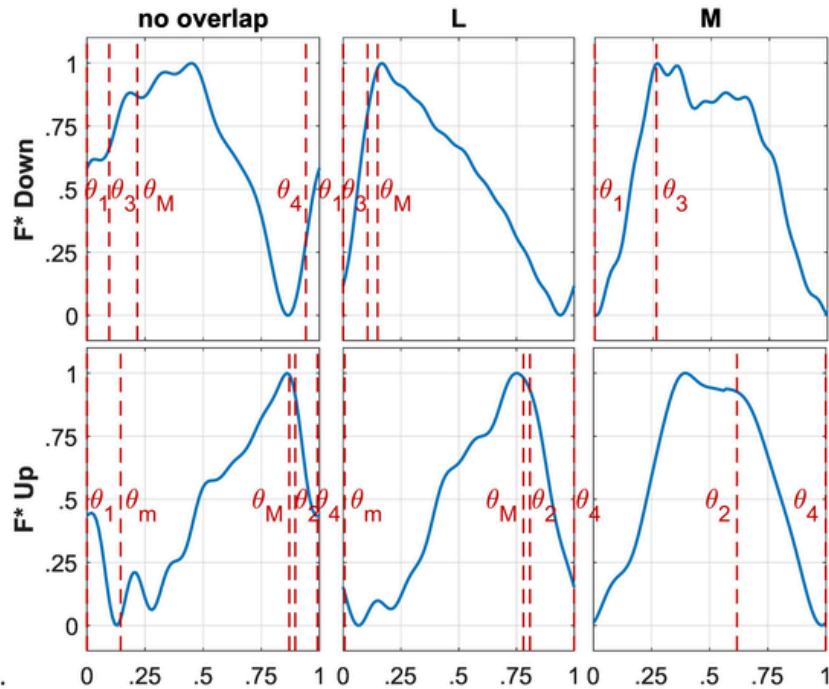


Fig. 17. Type III normalized  $F_y$  shapes (tests 31 to 33 in down-milling; tests 34 to 36 in up-milling).

and 0.007 mm for tool 2). Due to the small values obtained, it was assumed that tool runout did not significantly alter the surface error shape. The measured surface error profiles were compared with the analytical results of the proposed approach. In detail, the surface error profiles are presented in groups based on the type of single flute  $F_y$  shape (Fig. 18, Fig. 19, Fig. 20, Fig. 21, Fig. 22). In each chart the vertical axis represents the unity based normalized axial depth of cut  $Z^*$ , and the horizontal axis reports the unity based normalized surface error magnitude  $e^*$ . The equation expressing  $Z^*$  and  $e^*$  are presented as follows:

$$Z^* = z_k / ap \quad (40)$$

where  $z_k$  is the axial distance from the tooltip of a generic point  $k$  along the tool axis.

$$e^* = \frac{e_k - \min(e)}{\max(e) - \min(e)} \quad (41)$$

where  $e_k$  is the generic  $k$  value of the surface error  $e$  along  $ap$ , while  $\max(e)$  and  $\min(e)$  represent the maximum and minimum values of  $e$  along  $ap$ . In each chart the measured surface error profile (blue) and the analytical key points axial positions (red lines) are reported. The bottom red line ( $z_2^1$  in down-milling and  $z_1^1$  in up-milling) represents the bottom of the axial depth of cut ( $ap$ ), while the top red line ( $z_4^1$  in down-milling and  $z_3^1$  in up-milling) represents the top of the axial depth of cut ( $ap$ ).

Fig. 18 shows type Ia single flute  $F_y$  shape with three degrees of overlap, no overlap, low (L) and medium (M), for both down-milling (first row) and up-milling (second row). In down-milling, the surface

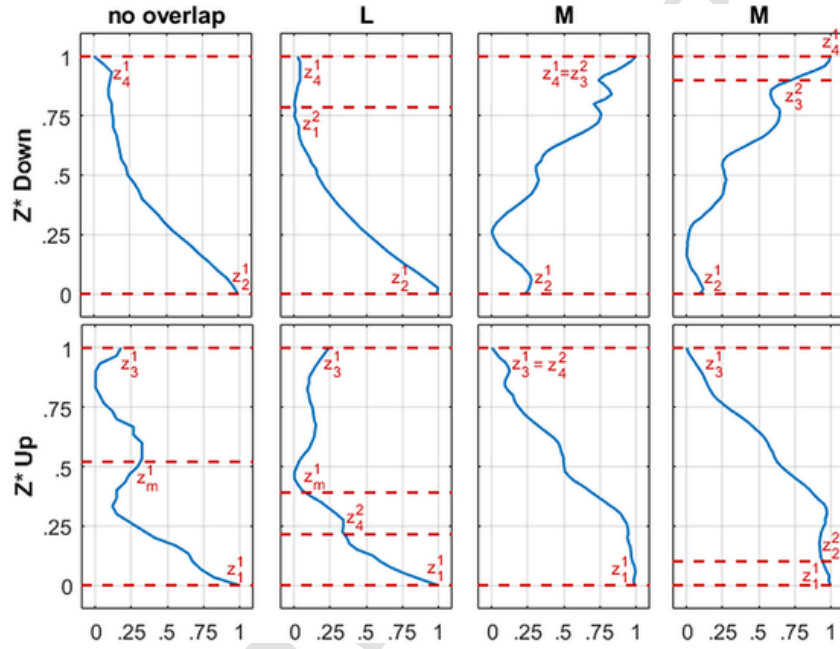


Fig. 18. Type Ia normalized surface error profiles (tests 1 to 4 in down-milling; tests 5 to 8 in up-milling).

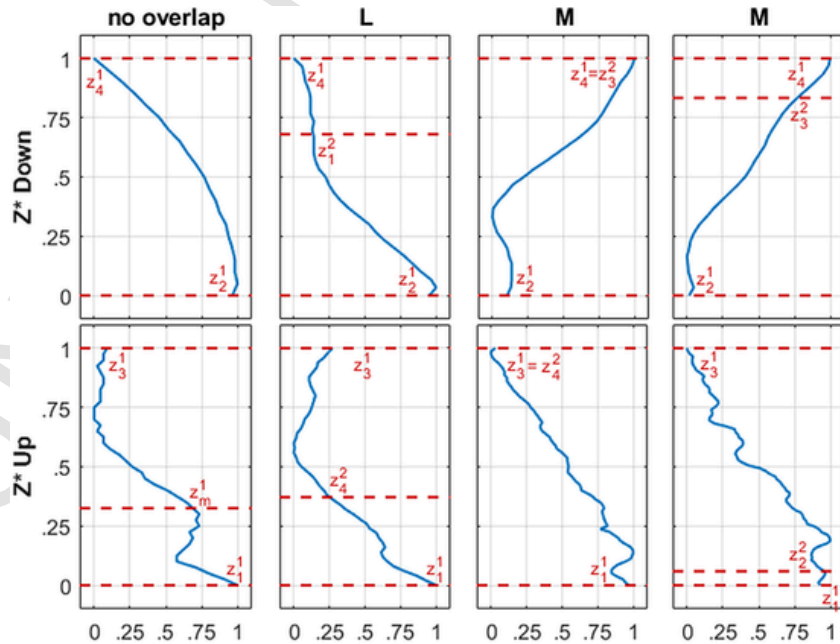


Fig. 19. Type Ib normalized surface error profiles (tests 9 to 12 in down-milling; tests 13 to 16 in up-milling).

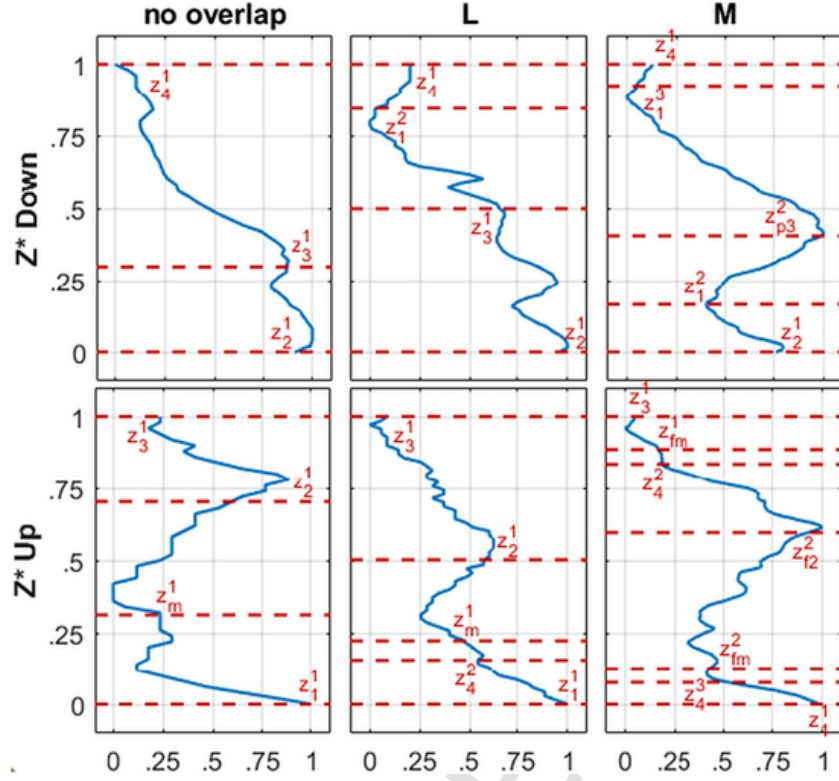


Fig. 20. Type IIa normalized surface error profiles (tests 17 to 19 in down-milling; tests 20 to 22 in up-milling).

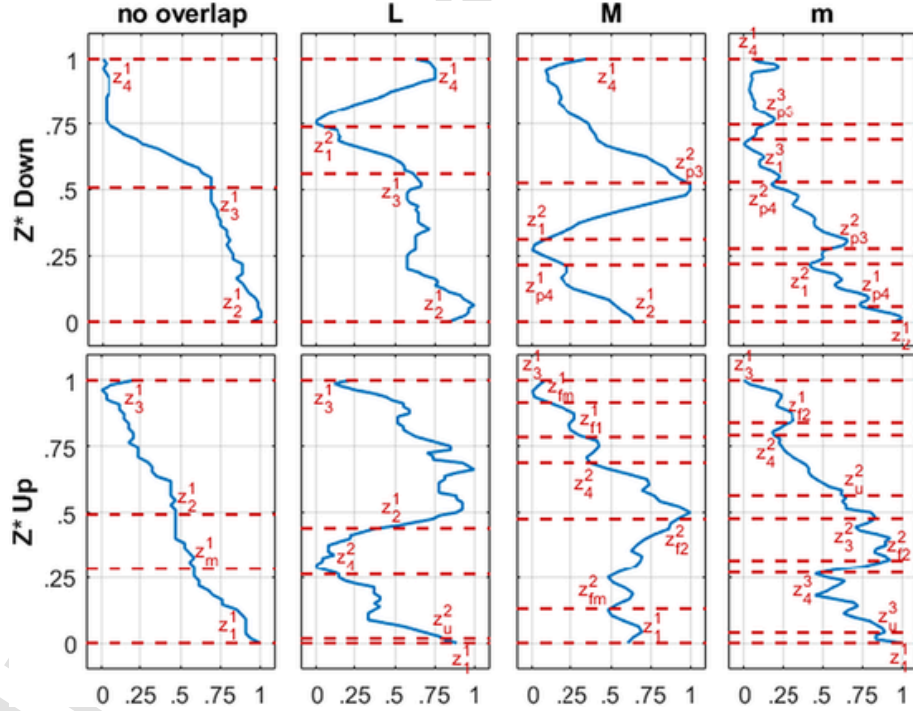


Fig. 21. Type IIb normalized surface error profiles (tests 23 to 26 in down-milling; tests 27 to 30 in up-milling).

generation range is delimited by the key angles  $\theta_2$  and  $\theta_4$  of the starting period of  $F_y$ , and they are defined through Eqs. (15) and (17). The starting period of  $F_y$  is referred to as “1”, and the key angles delimiting the surface generation range in down-milling are referred to as  $\theta_2^1$  and  $\theta_4^1$ . These two key angles identify the endpoints of the surface generating force shape, and, according to Eq. (34), they provide the axial positions  $z_2^1$  and  $z_4^1$ . These two axial positions are the endpoints of the ax-

ial depth of cut  $ap$  for any down-milling operations. For the no overlap configuration (test 1), the surface generation range is located within one period of  $F_y$  where the surface generating force shape is identified only by key angles  $\theta_2^1$  and  $\theta_4^1$ . Therefore, the surface error shape is described by only the key points representing the endpoints of the axial depth of cut, as it is confirmed by the experimental result. As the degree of overlap increases, and higher axial depths of cut are used, the



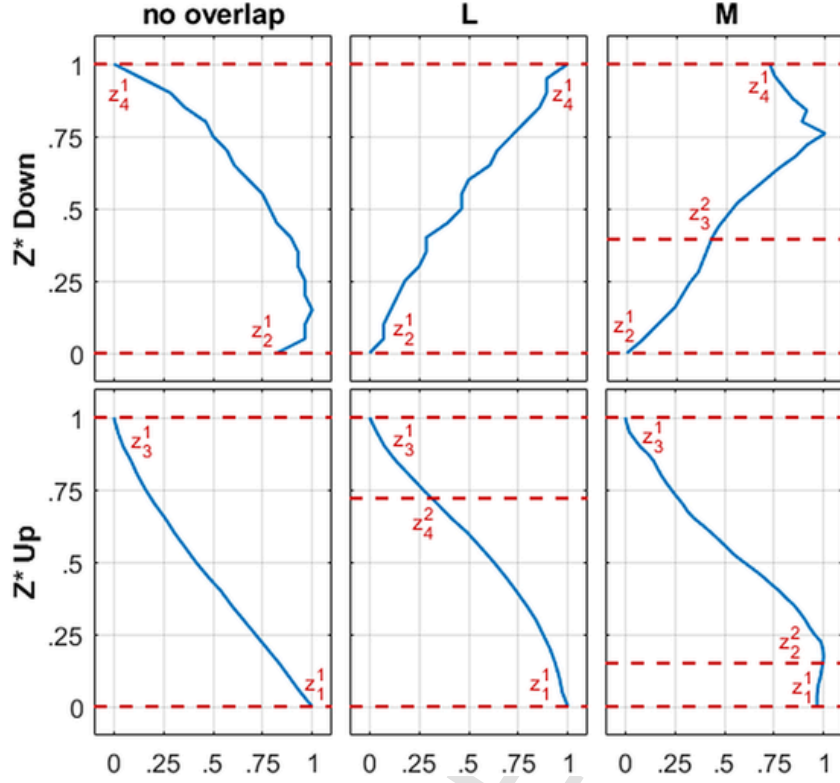


Fig. 22. Type III normalized surface error profiles (tests 31 to 33 in down-milling; tests 34 to 36 in up-milling).

amplitude of the surface generation range increases, while the amplitude of the  $F_y$  period decreases. For this reason, the surface generation range covers more periods of the  $F_y$  shape. In the low overlap configuration (test 2) two periods of  $F_y$  are located within the surface generation range, and in this range the only key angles identifying the surface generating force shape are  $\vartheta_2^1$  and  $\vartheta_4^1$  of the starting period, together with the key angle  $\vartheta_1$  of the first period following the starting one ( $\vartheta_{12}$ ). Therefore, the surface error shape is identified by the endpoints of the axial depth of cut ( $z_2^1$  and  $z_4^1$ ) and the key point related to  $\vartheta_1^2$ , which is referred to as  $z_1^2$ . In this configuration the measured surface error shape shows good agreement with the proposed analytical axial positions. In the medium overlap configuration (test 3), the surface generation range covers two periods of the  $F_y$ , but due to the cutting conditions adopted, the key angle  $\vartheta_4^1$  of the starting period is equal to the key angle  $\vartheta_3^2$  of the following period. Therefore, the surface generating force shape is characterized by  $\vartheta_1^1$  and two equal key angles ( $\vartheta_4^1$  and  $\vartheta_3^2$ ). Consequently, the surface error shape is identified by  $z_2^1$  and two equal positions ( $z_4^1$  and  $z_3^2$ ). The measured surface error and the analytical axial positions are in good agreement, but the measured surface error shows considerable fluctuations. These fluctuations are probably related to forced vibrations, which depending on the cutting parameters adopted, may add fluctuations to the surface error shape. In test 4, the situation is similar, but  $\vartheta_3^2$  is not equal to  $\vartheta_4^1$ . Therefore, the surface error shape is effectively identified by  $z_2^1$ ,  $z_4^1$  and  $z_3^2$ . However, due to the dynamic effects, fluctuations are present in the measured surface error making  $z_3^2$  difficult to highlight. In up-milling, the surface generation range is delimited by the key angles  $\vartheta_1$  and  $\vartheta_3$  of the starting period of  $F_y$ , and they are defined through Eqs. (14) and (16). The starting period of  $F_y$  is referred to as “1”, and the key angles delimiting the surface generation range in up-milling are referred to as  $\vartheta_1^1$  and  $\vartheta_3^1$ . These two key angles identify the endpoints of the surface generating force shape, and, according to Eq. (35), they provide the axial positions  $z_1^1$  and  $z_3^1$ . These two axial positions are the endpoints of the axial depth  $ap$  for any up-milling operations. In the no overlap configuration (test 5) the surface generation range is lo-

cated within one period of  $F_y$  where the surface generating force shape is identified by the key angles  $\vartheta_1^1$ ,  $\vartheta_m^1$  and  $\vartheta_3^1$ . Therefore, the surface error shape is described by the key points representing the endpoints of the axial depth of cut and the key point related to  $\vartheta_m^1$ , which is referred to as  $z_m^1$ . In this case despite the same fluctuations related to dynamic effects, there is a good match between the measured surface error shape and the analytical axial positions proposed. In the low overlap configuration (test 6) two periods of  $F_y$  are located within the surface generation range, and in this range the key angles identifying the surface generating force shape are the  $\vartheta_1^1$ ,  $\vartheta_m^1$  and  $\vartheta_3^1$  of the starting period along with the key angle  $\vartheta_4$  of the first period preceding the starting one ( $\vartheta_4^2$ ). Therefore, the surface error shape is identified by the endpoints of the axial depth of cut ( $z_1^1$  and  $z_3^1$ ) and the key points related to  $\vartheta_m^1$  and  $\vartheta_4^2$ , which are referred to as  $z_m^1$  and  $z_4^2$ . In this configuration, the measured surface error shape shows good agreement with the proposed analytical axial position, despite the fluctuations. In the medium overlap configuration (test 7), the same condition described for test 3 in down-milling occurs. Indeed, the surface generation range covers two periods of the  $F_y$ , but due to the cutting conditions adopted, the key angles  $\vartheta_4^2$  of the starting period and  $\vartheta_3^1$  of the preceding period are equal. Therefore, the surface error shape is identified by  $z_1^1$  and two equal axial positions  $z_3^1$  and  $z_4^2$ . In this case, measured surface error and the analytical axial positions are in good agreement, and fluctuations are less dominant. In test 8, two periods of  $F_y$  are located within the surface generation range, and the key angles identifying the surface generating force shape are  $\vartheta_1^1$ ,  $\vartheta_3^1$  and the key angle  $\vartheta_2$  of the period preceding the starting one ( $\vartheta_{22}$ ). Therefore, the surface error shape is identified by the endpoints of the axial depth of cut ( $z_1^1$  and  $z_3^1$ ) and the key point related to  $\vartheta_2^2$  ( $z_2^2$ ). However, due to the dynamic effects, measured surface error shows fluctuations which make  $z_2^2$  less recognizable.

Fig. 19 presents type Ib single flute  $F_y$  shape with three different degrees of overlap (no overlap, Low and Medium) in both down-milling and up-milling. In terms of surface error profile, the differences between type Ia and type Ib are minimal because the variation



in the  $F_y$  shape occurs outside the surface generation range. Therefore, the surface error profiles for type Ib resemble the ones for type Ia, and the same observations made for type Ia also apply to type Ib. However, in test 14, unlike test 6, the surface error shape is not characterized by  $z_m^1$  because  $\theta_m^1$  is not relevant for  $F_y$  shape as it was explained in force shape validation. Indeed, in test 6, due to the depths of cut adopted,  $z_4^2$  is lower than  $z_m^1$ , and Eq. (29) is verified. However, when Eq. (29) is not verified, as in test 14,  $z_4^2$  becomes higher than  $z_m^1$  deleting it.

Fig. 20 shows type IIa single flute  $F_y$  shape in three different configurations, no overlap, low overlap (L) and medium overlap (M) for both down-milling and up-milling. In down-milling for the no overlap configuration (test 17), the surface generation range is located within one period of  $F_y$  where surface generating force shape is identified by  $\theta_2^1$ ,  $\theta_3^1$  and  $\theta_4^1$ . Therefore, the surface error shape is characterized by  $z_2^1$  and  $z_4^1$ , which represent the endpoints of the axial depth of cut but also  $z_3^1$  which represents the key point axial position related to  $\theta_3^1$ . In this case, despite some fluctuations, a very good match is found between the proposed axial positions and the measured surface error shape. In the low overlap condition (test 18) the surface generation range covers two periods of  $F_y$ , and surface generating force shape is identified by the key angles  $\theta_2^1$ ,  $\theta_3^1$  and  $\theta_4^1$  of the starting period and the key angle  $\theta_1^2$  of the following period. Thus, the surface error shape is identified by the endpoints representing the axial depth ( $z_2^1$  and  $z_4^1$ ) and the axial positions  $z_3^1$  and  $z_1^2$  which are related to  $\theta_3^1$  and  $\theta_1^2$  respectively. For this test, the proposed analytical axial positions well agree with the measured surface error shape. In the medium overlap configuration (test 19) due to the high axial depth of cut adopted, the amplitude of the surface generation range is significantly high covering three periods of  $F_y$ . Therefore, the surface generating force shape is identified by  $\theta_2^1$  and  $\theta_4^1$  from the starting period,  $\theta_1^2$ ,  $\theta_{p3}^2$  from the first period following the starting one and  $\theta_1^3$  from the second period following the starting one. Consequently, the surface error shape is identified by the endpoints of the axial depth of cut ( $z_2^1$  and  $z_4^1$ ) together with  $z_1^2$ ,  $z_{p3}^2$  and  $z_1^3$  obtaining a good correspondence with the measured surface error shape. In up-milling, for the no overlap configuration (test 20), the same considerations made in down-milling apply also to up-milling. Indeed, the surface generation range covers only one period of  $F_y$  where the surface generating force shape is identified by  $\theta_1^1$ ,  $\theta_m^1$ ,  $\theta_2^1$  and  $\theta_3^1$ , but the first and the last key angle ( $\theta_1^1$  and  $\theta_3^1$ ) also identify the endpoints of the surface generation range. Therefore, the surface error shape is identified by the endpoints of the axial depth of cut ( $z_1^1$  and  $z_3^1$ ),  $z_m^1$  and  $z_2^1$ , which are related to  $\theta_m^1$  and  $\theta_2^1$  respectively. These four analytical positions show a good match with the measured surface error shape. In the low overlap configuration (test 21), following the same pattern, the surface generation range covers two periods of  $F_y$ , and the surface error shape is identified by the endpoints of the axial depth of cut,  $z_m^1$ ,  $z_2^1$ , which are related to the key angles  $\theta_m^1$  and  $\theta_2^1$  of the starting period, and  $z_4^2$ , which is related to the key angle  $\theta_4^2$  of the preceding period. These axial positions agree well with the measured surface error, and as previously explained the presence of  $z_m^1$  depends on Eq. (29) which is verified in this case. In the medium overlap configuration (test 22), the surface generation range covers three periods of  $F_y$ , and the key angles of all three periods identify the surface generating force shape. In detail, the surface generating force shape is characterized by three key angles ( $\theta_1^1$ ,  $\theta_3^1$ ,  $\theta_{fm}^1$ ) from the starting period, two key angles ( $\theta_{p2}^2$  and  $\theta_{fm}^2$ ) from the first period preceding the starting one, and one key angle ( $\theta_4^3$ ) from the second period preceding the starting one. Therefore, the surface error shape is identified by the axial depth of cut endpoints,  $z_{fm}^1$ ,  $z_{p2}^2$ ,  $z_{fm}^2$  and  $z_4^3$ . In this case, the measured surface error shape presents small fluctuations, however the found analytical axial positions well agree with the experimental shape.

In Fig. 21 type IIb single flute  $F_y$  shape with four different degrees of overlap, no overlap, low (L), medium (M) and Deep medium (m) is

shown. The first row shows the surface error profiles in down-milling while the second row shows the ones in up-milling (second row). In down-milling, for the no overlap and low overlap configurations (test 23 and test 24), the same consideration made for type IIa also apply to type IIb because type IIb differs from type IIa only for the higher axial depth of cut, which has an impact on the higher degrees of overlap. Indeed, for the medium overlap configuration (test 25) due to the lower axial depth of cut compared to test 19, the surface generation range covers only two periods of  $F_y$ , but Eq. (26) is verified, and the key angle  $\theta_{p4}^1$  becomes relevant for the  $F_y$  shape, as it was described in the force shape validation. Therefore, the surface generating force shape is identified by  $\theta_2^1$ ,  $\theta_4^1$  and  $\theta_{p4}^1$  from the starting period along with  $\theta_1^2$  and  $\theta_{p3}^2$  from the following period. Following Eq. (34), the obtained analytical axial positions ( $z_2^1$ ,  $z_3^1$ ,  $z_{p4}^1$ ,  $z_1^2$  and  $z_{p3}^2$ ) show good agreement with the measured surface error shape. In the deep medium overlap configuration (test 26), thanks to the higher axial depth of cut, the surface generation range covers three periods of  $F_y$ , and several key angles identify the surface generating force shape. Indeed, Eq. (26) is verified thus  $\theta_{p4}^1$  becomes relevant for the  $F_y$  shape, and the surface generating force shape is characterized by three key angles from the starting period ( $\theta_2^1$ ,  $\theta_4^1$  and  $\theta_{p4}^1$ ), three key angles ( $\theta_1^2$ ,  $\theta_{p3}^2$  and  $\theta_{p4}^2$ ) from the first period following the starting one, and two key angles ( $\theta_1^3$  and  $\theta_{p3}^3$ ) from the second period following the starting one. The several axial positions obtained by these key angles well agree with the measured surface error shape even if the measured profile presents small fluctuations related to dynamic effects. In up-milling, for the no overlap configuration (test 27) the axial positions obtained follow the same procedure described for test 20. However, due to the conservative cutting parameters adopted, cutting forces were low, and the measured surface error shape suffers from the ploughing of the material. For this reason,  $z_m^1$  and  $z_2^1$  cannot be identified on the altered measured surface error. In the low overlap, configuration (test 28), the surface generation range covers two period of  $F_y$ , but, unlike test 21, a higher number of key angles ( $\theta_u^2$  and  $\theta_4^2$ ) of the first period preceding the starting one identify the surface generating force shape. Indeed, with the same degree of overlap, a higher axial depth of cut was adopted, and the amplitude of surface generation range increased covering a wider portion of the second period of  $F_y$ . For this reason, the surface error shape is identified by the endpoints of the axial depth of cut ( $z_1^1$  and  $z_3^1$ ),  $z_2^1$ ,  $z_u^2$  and  $z_4^2$ . In this case, despite small fluctuations affecting the measured surface error shape, the analytical axial positions are in good agreement with the experimental result. In the medium overlap configuration (test 29), the surface generation range covers two periods of  $F_y$ , unlike test 22, because a lower axial depth of cut was used. However, due to the cutting conditions adopted, both Eqs. (26) and (30) are verified therefore the key angle  $\theta_{f1}$  and  $\theta_{fm}$  become relevant for the  $F_y$  shape. Consequently, the surface generating force shape is identified by four key angles ( $\theta_1^1$ ,  $\theta_{f1}^1$ ,  $\theta_{fm}^1$  and  $\theta_3^1$ ) from the starting period and three key angles ( $\theta_{fm}^2$ ,  $\theta_{p2}^2$  and  $\theta_4^2$ ) from the preceding period. The axial positions obtained from these key angles present a good match with the measured surface error shape even if it is affected by small fluctuations. In the deep medium overlap condition (test 30) the surface generation range covers three periods of  $F_y$ , and Eq. (33) is verified with cutting parameters adopted making  $\theta_u$  relevant in each period. Therefore, the surface generating force shape is identified by three key angles from the starting period ( $\theta_1^1$ ,  $\theta_3^1$  and  $\theta_{p2}^1$ ), three key angles ( $\theta_3^2$ ,  $\theta_u^2$  and  $\theta_4^2$ ) from the first period preceding the starting one, and two key angles ( $\theta_u^3$  and  $\theta_4^3$ ) from the second period preceding the starting one. Following Eq. (35), the obtained axial positions are in very good agreement with the measured surface error despite the fluctuations affecting the measured profile.

In Fig. 22 type III single flute  $F_y$  shape with three different degrees of overlap (no overlap, Low and Medium) is reported for both down-milling (first row) and up-milling (second row). In down-milling, for the type III/no overlap combination (test 31), the amplitude of the sur-

face generation range is very small, and it covers one period of  $F_y$  where the surface generating force shape is identified only by the key angles  $\vartheta_2^1$  and  $\vartheta_4^1$ . Therefore, the surface error shape is described by only the key points representing the endpoints of the axial depth of cut as it is confirmed by the experimental result. In the no overlap configuration (test 32), despite the higher degree of overlap, the surface generation range covers only one period of  $F_y$  where the surface generating force shape is identified only by the key angles  $\vartheta_2^1$  and  $\vartheta_4^1$ . Therefore, in this case, the same axial positions as the previous case are obtained. However, despite the same good agreement with the experimental results, the two measured surface errors are different because the slope of the falling edge of the  $F_y$  shape changes from test 31 to test 32 on account of the overlap. In the medium overlap condition (test 33). The surface generation range covers two periods, and, within this range, the surface generating force shape is identified by  $\vartheta_2^1$  and  $\vartheta_4^1$  from the starting period and  $\vartheta_3^1$  from the following period. Therefore, the surface error shape is identified by  $z_2^1$ ,  $z_4^1$  and  $z_3^2$ . However, due to the low axial depth of cut, the surface generation range is extremely small, and side effects which may affect measured the surface error becomes significant. Because of this, the measured surface error shape is altered, and  $z_3^2$  is not highlighted. In up-milling, for the no overlap configuration (test 34), the small surface generation range covers only one period of  $F_y$ , and the surface generating force shape is identified by only the key angles  $\vartheta_1^1$  and  $\vartheta_3^1$ . Therefore, the surface error shape is described by only the key points representing the endpoints of the axial depth of cut, as it is confirmed by the experimental result. In the low overlap configuration (test 35) two periods of  $F_y$  are located within the surface generation range, and the key angles identifying the surface generating force shape are  $\vartheta_1^1$ ,  $\vartheta_3^1$  and the key angle  $\vartheta_4$  of the period preceding the starting one ( $\vartheta_4^2$ ). Therefore, the surface error shape is identified by the endpoints of the axial depth of cut ( $z_1^1$  and  $z_3^1$ ) and the key point related to  $\vartheta_4^2$  ( $z_4^2$ ). However, due to the dynamic effects, measured surface error shows fluctuations which make  $z_4^2$  not recognizable. In the medium overlap configuration (test 36) the surface generation range covers two periods of  $F_y$ , and within this range the surface generating force shape is identified by  $\vartheta_1^1$ ,  $\vartheta_3^1$  and  $\vartheta_2^2$ . Therefore, the surface error shape is identified by the endpoints of the axial depth of cut ( $z_1^1$  and  $z_3^1$ ) and  $z_4^2$ . Despite small deviations, the analytical key points axial positions well identify the measured surface error shape.

Generally, the proposed analytical axial positions effectively identify the surface error shape for any type/degree of overlap combination. However, for the certain combinations the measured surface error shapes shows fluctuations which may hide some of the proposed analytical positions. These fluctuations are probably related to the dynamic effects, which probably depends on the frequency content of  $F_y$  in the specific type/degree of overlap condition. However, it is interesting to note that with high axial depths of cut, measured surface errors still show fluctuations, but the proposed analytical positions still identify accurately the measured surface error shape. Therefore, the proposed formulations could represent an effective tool to increase the productivity of milling operations.

#### 4.4. Application to surface error prediction

The proposed formulations were applied to a predictive method to evaluate the surface error. In detail, the method considered is presented in [28], and it evaluates the surface error at  $i$  point due to the  $dF_y$  cutting force acting on point  $j$  with the following equation:

$$e_y(i, j) \begin{cases} \frac{dF_y v_i^2}{6EI} (3v_j - v_i) & 0 < v_i < v_j \\ -\frac{dF_y v_j^2}{6EI} (3v_i - v_j) & v_j < v_i \end{cases} \quad (42)$$

$$v_i = l - z_i \quad (43)$$

$$v_j = l - z_j \quad (44)$$

where  $l$  represents the tool overhang, while  $z_i$  and  $z_j$  are the distances from the tooltip of point  $i$  and point  $j$ , respectively. Instead EI represents the product between the Young modulus and the moment of Inertia for the endmill considered. Finally, the total predicted surface error  $e_i$  at the  $z_i$  position from the tooltip is found as follows:

$$e_i = \sum_j^m e_y(i, j) \quad (45)$$

where  $m$  is the number of points composing the axial depth of cut.

The proposed formulations are used to evaluate the static deflections only at the  $z_i$  positions corresponding to the key points instead of computing the static deflection for all the  $z_i$  positions composing the axial depth of cut as in [28]. Therefore, the number of calculations needed is considerably reduced without compromising the accuracy of the surface error prediction. This application was tested with some of the experimental error profiles obtained from the milling tests listed in Section 4.1 (Tests 4, 19, 26, 33 for down-milling and tests 8, 22, 30, 36 for up-milling). The EI values for the two endmills were found through Eq. (42) starting from two experimental static stiffness values: 4040.9 N/mm for tool 1 at 3 mm from the tooltip and 2304 N/mm for tool 2 at 5 mm from the tooltip. The comparisons between the predicted surface error profile and the measured one are shown in Fig. 23. In each chart the vertical axis  $Z^*$  represents the unity based normalized axial depth of cut, while the horizontal axis reports surface error magnitude.

The comparison shows that the evaluation of the tool static deflection only in correspondence to the key points axial positions is a valid method to effectively reproduce the surface error profile. In detail, it is interesting to note that even if some of the proposed analytical positions cannot be identified on the measured surface error shape, their use for the surface error prediction helps increasing the accuracy of the prediction, as it can be seen in test 4, 8 and 33. Moreover, for type III with medium overlap (test 36), the predicted surface error differs significantly from the measured one in terms of magnitude. This deviation could be due to an underestimation of the tool 2 flexibility or to dynamic effects which could be relevant especially at high spindle speed as the one tested using the tool 2.

## 5. Conclusions

The surface error caused by the tool static deflection in peripheral milling varies along the axial depth of cut and it presents a certain shape. This shape is strictly related to the shape of the resultant of the cutting forces along the perpendicular to the feed direction ( $F_y$ ). However, the shape of  $F_y$  is not unique, and it changes according to the cutting strategy, tool geometry and cutting parameters. Therefore, the surface error shape varies according to the same factors.

In this paper a comprehensive picture of the surface error shape is proposed. The shape of  $F_y$  was investigated through key points which are identified in the engagement angle domain  $\vartheta$  by key angles. These key angles were defined analytically with dedicated equations for all the possible shapes which  $F_y$  may assume. Moreover, these key angles were exploited to obtain the axial positions which characterize the surface error shape with additional equations. Both the key angles and the axial position analytically obtained were experimentally validated through several cutting tests in a wide range of different  $F_y$  shapes. The results show that the equations identify accurately the shape of both  $F_y$  and the surface error in different cutting conditions.

Furthermore, as an application, the equations proposed were coupled with an established tool deflection model to predict surface error reducing the number of axial positions where the tool deflection is evaluated. The predicted surface error was compared with some of the experimental results previously obtained from the cutting tests proving that the proposed formulations are a suitable tool to effectively predict

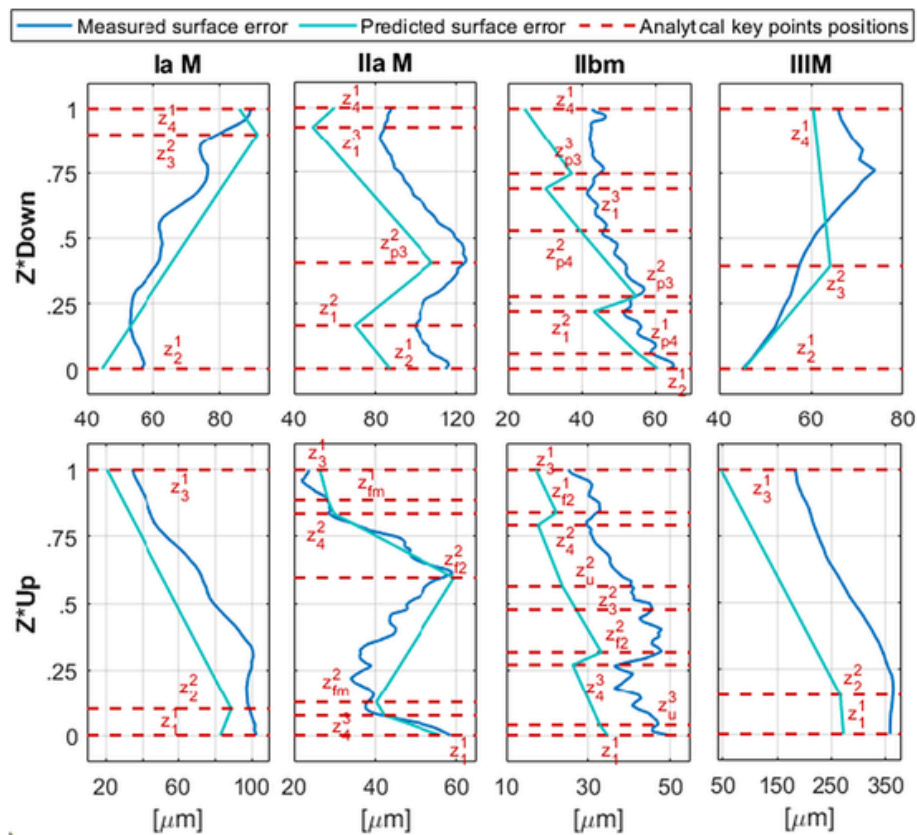


Fig. 23. Comparison between measured and predicted surface error (tests 4, 19, 26, 33 in down-milling; tests 8, 22, 30, 36 in up-milling).

surface errors even for cutting operations with high depths of cut. Similarly, the proposed formulations could be potentially applied to predictive approach for thin-walled components deflection in order to accurately estimate the workpiece/tool couple deflection considering only a reduced number of points (such as the one proposed in [5]). As well as this, the equations proposed in this paper may be exploited to reduce the numbers of points for in-line surface measurements saving time for quality control. Finally, since the equations proposed depend on cutting parameters and tool geometry, they could help preselecting tool geometry and cutting parameters to obtain a certain surface error shape.

#### Funding

No funding supported this research.

#### Availability of data and material

No data are available.

#### Code availability

No code is available.

#### CRediT authorship contribution statement

Conceptualization and Methodology A.S., N.G., L.M.; Investigation and Validation N.G., L.M.; Writing - Original Draft L.M.; Writing - Review & Editing and Supervision, N.G.; Supervision A.S., N.G.; Project administration and Funding acquisition, G.C.

#### Declaration of competing interest

The authors declare that they have no known competing financial interests or personal relationships that could have appeared to influence the work reported in this paper.

#### Acknowledgement

The authors would like to thank Machine Tool Technology Research Foundation (MTTRF) and its supporters for the loaned machine tool (DMG MORI DMU 75 MonoBlock).

#### References

- [1] Zhang X, Zhang W, Zhang J, Pang B, Zhao W. Systematic study of the prediction methods for machined surface topography and form error during milling process with flat-end cutter. *Proc Inst Mech Eng B J Eng Manuf* 2019;233:226–42. <https://doi.org/10.1177/0954405417740924>.
- [2] Liu C, Gao L, Wang G, Xu W, Jiang X, Yang T. Online reconstruction of surface topography along the entire cutting path in peripheral milling. *Int J Mech Sci* 2020; 185:105885. <https://doi.org/10.1016/j.ijmecsci.2020.105885>.
- [3] Li Z, Yan Q, Tang K. Multi-pass adaptive tool path generation for flank milling of thin-walled workpieces based on the deflection constraints. *J Manuf Process* 2021; 68:690–705. <https://doi.org/10.1016/j.jmapro.2021.05.075>.
- [4] Hou Y, Zhang D, Mei J, Zhang Y, Luo M. Geometric modelling of thin-walled blade based on compensation method of machining error and design intent. *J Manuf Process* 2019;44:327–36. <https://doi.org/10.1016/j.jmapro.2019.06.012>.
- [5] Grossi N, Scippa A, Croppi L, Morelli L, Campatelli G. Adaptive toolpath for 3-axis milling of thin walled parts. *MM SJ* 2019;2019:3378–85. <https://doi.org/10.17973/MMSJ.2019.11.2019096>.
- [6] Davis TA, Shin YC, Yao B. Adaptive robust control of machining force and contour error with tool deflection using global task coordinate frame. *Proc Inst Mech Eng B J Eng Manuf* 2018;232:40–50. <https://doi.org/10.1177/0954405416654100>.
- [7] Scippa A, Grossi N, Campatelli G. FEM based cutting velocity selection for thin walled part machining. *Procedia CIRP* 2014;14:287–92. <https://doi.org/10.1016/j.procir.2014.03.023>.
- [8] Schmitz TL, Mann BP. Closed-form solutions for surface location error in milling. *Int J Mach Tool Manuf* 2006;46:1369–77. <https://doi.org/10.1016/j.jmachtools.2005.10.007>.

- [9] Wang D, Löser M, Luo Y, Ihlenfeldt S, Wang X, Liu Z. Prediction of cumulative surface location error at the contact zone of in-process workpiece and milling tool. *Int J Mech Sci* 2020;177:105543. <https://doi.org/10.1016/j.ijmecsci.2020.105543>.
- [10] Nishida I, Okumura R, Sato R, Shirase K. Cutting force and finish surface simulation of end milling operation in consideration of static tool deflection by using voxel model. *Procedia CIRP* 2018;77:574–7. <https://doi.org/10.1016/j.procir.2018.08.218>.
- [11] Bhattacharya A, Bera TK, Thakur A. On cutter deflection profile errors in end milling: modeling and experimental validation. *Null* 2015;30:1042–59. <https://doi.org/10.1080/10426914.2014.973598>.
- [12] Costes JP, Moreau V. Surface roughness prediction in milling based on tool displacements. *J Manuf Process* 2011;13:133–40. <https://doi.org/10.1016/j.jmapro.2011.02.003>.
- [13] Yuan L, Zeng S, Chen Z. Simultaneous prediction of surface topography and surface location error in milling. *Proc Inst Mech Eng C J Mech Eng Sci* 2015;229:1805–29. <https://doi.org/10.1177/0954406214547401>.
- [14] Jalili Saffar R, Razfar MR, Zarei O, Ghassemieh E. Simulation of three-dimension cutting force and tool deflection in the end milling operation based on finite element method. *Simul Model Pract Theory* 2008;16:1677–88. <https://doi.org/10.1016/j.simpat.2008.08.010>.
- [15] Islam MN, Lee HU, Cho D-W. Prediction and analysis of size tolerances achievable in peripheral end milling. *Int J Adv Manuf Technol* 2008;39:129–41. <https://doi.org/10.1007/s00170-007-1188-4>.
- [16] Desai KA, Rao PVM. On cutter deflection surface errors in peripheral milling. *J Mater Process Technol* 2012;212:2443–54. <https://doi.org/10.1016/j.jmatprotec.2012.07.003>.
- [17] Denkena B, Dittich M-A, Uhlich F. Augmenting milling process data for shape error prediction. *Procedia CIRP* 2016;57:487–91. <https://doi.org/10.1016/j.procir.2016.11.084>.
- [18] Budak E. Analytical models for high performance milling. Part I: cutting forces, structural deformations and tolerance integrity. *Int J Mach Tool Manuf* 2006;46:1478–88. <https://doi.org/10.1016/j.ijmachtools.2005.09.009>.
- [19] Agarwal A, Desai KA. Effect of workpiece curvature on axial surface error profile in flat end-milling of thin-walled components. *Procedia Manuf* 2020;48:498–507. <https://doi.org/10.1016/j.promfg.2020.05.074>.
- [20] Liu X-W, Cheng K, Webb D, Luo X-C. Prediction of cutting force distribution and its influence on dimensional accuracy in peripheral milling. *Int J Mach Tool Manuf* 2002;42:791–800. [https://doi.org/10.1016/S0890-6955\(02\)00016-0](https://doi.org/10.1016/S0890-6955(02)00016-0).
- [21] Wang M-Y, Chang H-Y. A simulation shape error for end milling AL6061-T6. *Int J Adv Manuf Technol* 2003;22:689–96. <https://doi.org/10.1007/s00170-003-1570-9>.
- [22] Yun W-S, Ko JH, Cho D-W, Ehmann KF. Development of a virtual machining system, part 2: prediction and analysis of a machined surface error. *Int J Mach Tool Manuf* 2002;42:1607–15. [https://doi.org/10.1016/S0890-6955\(02\)00138-4](https://doi.org/10.1016/S0890-6955(02)00138-4).
- [23] Chiang HN, Junz Wang JJ. Generating mechanism and formation criteria of kinked surface in peripheral end milling. *Int J Mach Tool Manuf* 2011;51:816–30. <https://doi.org/10.1016/j.ijmachtools.2011.07.004>.
- [24] Yang L, DeVor RE, Kapoor SG. Analysis of force shape characteristics and detection of depth-of-cut variations in end milling. *J Manuf Sci Eng* 2005;127:9.
- [25] Rao VS, Rao PVM. Tool deflection compensation in peripheral milling of curved geometries. *Int J Mach Tool Manuf* 2006;46:2036–43. <https://doi.org/10.1016/j.ijmachtools.2006.01.004>.
- [26] Bhattacharyya A, Schueller JK, Mann BP, Ziegert JC, Schmitz TL, Taylor FJ, et al. A closed form mechanistic cutting force model for helical peripheral milling of ductile metallic alloys. *Int J Mach Tool Manuf* 2010;50:538–51. <https://doi.org/10.1016/j.ijmachtools.2010.03.003>.
- [27] Sultan AA, Okafor AC. Effects of geometric parameters of wavy-edge bull-nose helical end-mill on cutting force prediction in end-milling of Inconel 718 under MQL cooling strategy. *J Manuf Process* 2016;23:102–14. <https://doi.org/10.1016/j.jmapro.2016.05.015>.
- [28] Altintas Y. *Manufacturing Automation*. Second. United States of America, Cambridge University Press; 2012.
- [29] Ruben MA, Schmitz TL. Mechanistic force model coefficients: a comparison of linear regression and nonlinear optimization. *Precis Eng* 2016;45:311–21. <https://doi.org/10.1016/j.precisioneng.2016.03.008>.
- [30] Scippa A, Sallese L, Grossi N, Campatelli G. Improved dynamic compensation for accurate cutting force measurements in milling applications. *Mech Syst Signal Process* 2015;54–55:314–24. <https://doi.org/10.1016/j.ymssp.2014.08.019>.
- [31] Grossi N, Sallese L, Scippa A, Campatelli G. Speed-varying cutting force coefficient identification in milling. *Precis Eng* 2015;42:321–34. <https://doi.org/10.1016/j.precisioneng.2015.04.006>.